ELSEVIER

Journal of Nuclear Materials 257 (1998) 213–255

journal of nuclear materials

Thermodynamic modelling of the O–U–Zr system

P.Y. Chevalier *, E. Fischer

THERMODATA-INPG-CNRS (Unité Mixte de Service n° 818 THERMA), BP 66, F-38402 Saint Martin d'Hères cedex, France

Received 12 November 1997; accepted 4 June 1998

Abstract

To increase the basic knowledge of key phenomena which occur during the molten corium–concrete interaction (MCCI) resulting from the event of a severe accident in a nuclear power plant, we are developing a thermodynamic database for the corium (TDBCR) including the main materials involved. The first step of the accident is the core degradation, resulting from the interaction of the fuel (UO_2) with the zircaloy (98 wt% Zr). That is why the thermodynamic modelling of the fundamental O–U–Zr system is performed from a critical assessment of all the available experimental information. Optimized Gibbs energy parameters are given, and comparison between calculated and experimental equilibrium phase diagrams or thermodynamic properties is presented both for binary sub-systems and the ternary one, by means of isothermal (up to 3300 K) and isopleth sections of particular interest. The extent of the O–U liquid miscibility gap into the ternary system is especially discussed.

1. Introduction

Since 1989, in the framework of the nuclear reactor safety, we are interested in the thermodynamic modelling of a very complex mixture called 'corium', resulting from the thermochemical interaction of the different materials present in a pressurized water reactor (PWR). Particularly, in the unlikely event of a severe accident, if the reactor core melts through the vessel and slumps into the concrete reactor cavity, the phenomenon is called molten corium–concrete interaction (MCCI).

For that reason, we are developing a thermodynamic database for the corium (TDBCR), represented at this time by a 14-component system Ag–Al–Ba–Ca–Fe–In–La–Mg–O–Ru–Si–Sr–U–Zr for the condensed phases. It includes the main interacting materials, i.e. fuel (UO_2), zircaloy (Zr), steel structures (Fe), control rods (Ag, In), fission products (Ba, La, Ru, Sr) and concrete (Al_2O_3, CaO, FeO, Fe_2O_3, MgO, SiO_2). The thermodynamic modelling and critical assessment of all the binary and the most important higher-order sub-systems (metallic, oxide, metal–oxide/oxygen) is in completion and was recently presented in a general view [1]. The complex gas phase and other substances were taken from the Thermodata substance database [2].

During the first step of the accident, in which the core degradation is uncontrolled, the fuel rods melt and interact with other materials. When temperature increases, one possible phenomenon is the reduction of UO_2 by a reaction with the metallic zircaloy. A partial disintegration of UO_2 follows, leading to a metal–oxide mixture containing a ceramic $(U, Zr)O_{2\pm x}$ at sufficiently high oxygen potential. Thus, a precise knowledge of the ternary metal–oxygen O–U–Zr system is needed and its thermodynamic modelling has been performed from a critical assessment of all the available experimental information, equilibrium phase diagram and thermodynamic properties. An appropriate optimization procedure was used for the binary O–U, O–Zr, U–Zr or pseudo-binary UO_2–ZrO_2 sub-systems. For the ternary system, thermodynamic considerations have been argued for justifying the necessity of including ternary parameters or not, without using a general ternary optimization procedure.

In this work, we first describe the general principle of the thermodynamic modelling and assessment method. Then we present for each system (binary, pseudo-binary and ternary), the equilibrium phases, the complete

* Corresponding author.

0022-3115/98/$ – see front matter
PII: S0022-3115(98)00450-4

analysis of the available experimental information, concerning both phase diagram and thermodynamics, and finally, the detailed optimization results: on the one hand, optimized Gibbs energy parameters of all condensed substance and solution phases are annexed, and constitute a part of the TDBCR; on the other hand, phase diagrams and specific thermodynamic properties of all the optimized sub-systems have been calculated and compared to the experimental ones. Isothermal sections (1073–2973 K) or isopleth section of particular interest of the O–U–Zr phase diagram have been calculated and compared to the experimental information. The controversial limit of solubility in U–Zr liquid alloys and the extent of the O–U liquid miscibility gap into the ternary system at high temperature and zirconium content are discussed.

2. Thermodynamic modelling

2.1. Substances

In the classical substance databases, the fundamental thermodynamic properties stored for a substance are the enthalpy of formation $\Delta H^{\circ}_{f,298.15\ \mathrm{K}}$ and the entropy at room temperature $S^{\circ}_{298.15\ \mathrm{K}}$, the heat capacity C°_{p} at constant pressure varying versus temperature T, expressed in Kelvin, according to the relation (1), and the transition enthalpy L_{tr} if the substance shows a structural transformation at the temperature T_{tr}.

$$C^{\circ}_{p} = C_k + D_k T + E_k T^2 + F_k T^{-2} + \cdots (+G_k T^3 + H_k T^4 + I_k T^6 + J_k T^{-10} + L_k T^{-3} + M_k T^{-4}) \quad \text{for } T_k < T < T_{k+1}. \tag{1}$$

In the format used for phase diagrams calculations, the stored quantity is the Gibbs energy of the substance Φ, $G - H_{\mathrm{SER}}$, referred to a given reference state. SER means 'stable element reference' and is defined by the use of $H_{298.15\ \mathrm{K}}$ and $S_{\mathrm{O\ K}}$ for the stable state of the pure elements at 298.15 K and 1 bar. It is possible to calculate directly this quantity from the fundamental thermodynamic values, and reciprocally.

$$G - H_{\mathrm{SER}} = a_k + b_k T + c_k T \operatorname{Log} T + d_k T^2 + e_k T^3 + f_k T^{-1} + \cdots (+g_k T^4 + h_k T^5 + i_k T^7 + j_k T^{-9} + k_k \operatorname{Log} T + l_k T^{-2} + m_k T^{-3}) \quad \text{for } T_k < T < T_{k+1}. \tag{2}$$

In this expression, the coefficients $c, d, e, f, \ldots$ are connected to those of the heat capacity, while a and b are two integration constants depending on all the fundamental thermodynamic values. The points of suspension mean that these extra terms may be added if necessary, and are often used for extrapolation outside the stable domain.

In some cases, the heat capacity is unknown, and is estimated by the Neuman–Koop rule. In this case, the Gibbs energy, referred to the pure elements with a given structure (ref(1),... ref(i)), varies linearly versus temperature according to the simple relation

$$\Delta G = G - \sum x_i G_i^{\circ(\mathrm{ref(i)})} = a + bT, \tag{3}$$

where a and b correspond directly to ΔH and $-\Delta S$ which are independent of temperature.

2.2. Solutions

In a general way, the Gibbs energy of a condensed solution phase is the sum of several terms: reference, ideal, excess and magnetism or ordering in some cases.

$$G = G^{\mathrm{Ref}} + G^{\mathrm{Id}} + G^{\mathrm{Ex}} (+G^{\mathrm{Mag}} + G^{\mathrm{Ord}}). \tag{4}$$

In this work, we have used for the solid and liquid solution phase the general multi-sublattice model [4]

$$G^{\mathrm{Ref}} = \sum_{\mathrm{r}} P_{\mathrm{r}}(Y)\, {}^{\circ}G_r, \tag{5}$$

where ${}^{\circ}G_{\mathrm{r}}$ represents the Gibbs energy of all reference substances, obtained by making all the possible permutations on the different sub-lattices and by assuming successively that each sub-lattice is completely fulfilled by only one component. $P_{\mathrm{r}}(Y)$ is the corresponding product of site fractions from the Y matrix: $Y = (y_{\mathrm{i}}^{\mathrm{sl}})$, atomic fractions of the component i (pure or associate species) on the sub-lattice sl.

$$G^{\mathrm{Id}} = RT \sum_{\mathrm{sl}} Ns^{\mathrm{sl}} \sum y_i^{\mathrm{sl}} \operatorname{Log} y_i^{\mathrm{s}}. \tag{6}$$

Ns^{sl} is the number of sites of the sub-lattice sl, R the perfect gas constant.

In the one and two-sublattice model, the excess Gibbs energy for the ternary phases is equal to

$$G^{\mathrm{Ex}} = \sum G^{\mathrm{Ex}}(\mathrm{binary}) + G^{\mathrm{Ex}}(\mathrm{ternary}). \tag{7}$$

The expressions (8) and (9) are used for one lattice, Eqs. (10) and (11) for two sub-lattices:

$$G^{\mathrm{Ex}}(\mathrm{binary}) = \sum_j \sum_k y_j y_k L_{j,k}$$
$$L_{j,k} = \sum_v L_{j,k}^{(v)} (y_j - y_k)^v, \tag{8}$$

$$G^{\mathrm{Ex}}(\mathrm{ternary}) = \sum_i \sum_j \sum_k y_i y_j y_k$$
$$L_{i,j,k} L_{i,j,k} = y_i L^1_{i,j,k} + y_j L^2_{i,j,k} + y_k L^3_{i,j,k}, \tag{9}$$

$$G^{\mathrm{Ex}}(\mathrm{binary}) = \sum_l \sum_j \sum_k y_l y_j y_k L_{j,k:l}$$
$$L_{j,k:l} = \sum_v L_{j,k:l}^{(v)} (y_j - y_k)^v, \tag{10}$$

$$G^{\mathrm{Ex}}(\mathrm{ternary}) = \sum_i \sum_j \sum_k \sum_l y_i y_j y_k y_l L_{i,j,k:l}$$
$$L_{i,j,k:l} = y_i L^1_{i,j,k:l} + y_j L^2_{i,j,k:l} + y_k L^3_{i,j,k:l} \tag{11}$$

$L_{j,k}$ and $L_{i,j,k}$, or $L_{j,k:l}$ and $L_{i,j,k:l}$ represent the binary and ternary interaction parameters between the components i, j and k of one sublattice, the second sublattice (if existing) being supposed completely fulfilled by the component l. These parameters vary with temperature similarly to relation (2). The binary interaction parameters are described by using a Redlich–Kister type polynomial expression [5].

2.3. Assessment method

The values used for the lattice-stabilities of the pure condensed elements have been taken from the SGTE ('Scientific Group Thermodata Europe') database [6,7], for the following stable or metastable structures: U(ort_A20, tet, bcc_A2, L), O(L), Zr(bcc_A2, hcp_A3, L). The thermodynamic data of pure oxides UO_2(fcc_C1, L) and ZrO_2(mon, tet, fcc_C1, L) have been assessed separately. The values for other metastable structures needed in some solid solution phases have been estimated in this study: O(fcc_C1), U(fcc_C1), Zr(fcc_C1), O_2U_1(tet, mon).

The critical assessment of the coefficients, $a_k, b_k, c_k, d_k, e_k, f_k, \ldots$ for any other binary stoichiometric substance, and of the binary interaction parameters $L^{(v)}_{j,k}$ and $L^{(v)}_{j,k:l}$ for a binary or pseudo-binary solution, was performed for each binary O–U, O–Zr and U–Zr or pseudo-binary UO_2–ZrO_2 subsystem by using the optimization program developed by Lukas et al. [3], which allows to take into account simultaneously all the available experimental information, equilibrium phase diagram and thermodynamic properties.

For the O–U system, experimental results concerning the solubility of O in liquid uranium are very scattered. High solubility leads to a small liquid miscibility gap at high temperature, and inversely small solubility gives an enlarged liquid miscibility gap at high temperature. These important features of the phase diagram are controlled by the binary interaction parameter $L[O_2U_1, U_1]\langle L\rangle$. By waiting a final answer to the selection of experimental data, two different optimizations (a: high oxygen solubility in liquid uranium; b: small) will be discussed in the Section 3.1.

For the O–U–Zr ternary system, most of the parameters required by the used models are those of the binary or pseudo-binary subsystems. Only one ternary interaction parameter between uranium and zirconium has to be evaluated for each solid solution phase fcc_C1, hcp_A3 and bcc_A2, on the fictive metallic sublattice for the oxide phase ($L[Va_1]_2$ $[U_1, Zr_1]_1\langle$fcc_C1$\rangle$), and on the fictive oxide sublattice for the metallic phases ($L[O_1]_2$ $[U_1, Zr_1]_1\langle$hcp_A3$\rangle$, $L[O_1]_3$ $[U_1, Zr_1]_1\langle$bcc_A2$\rangle$). Due to the scarcity and inaccuracy of experimental information on one hand and the weak contribution of these parameters to the Gibbs energy on the other hand, they have been supposed to be equal to the corresponding parameters on the real sublattice ($L[O_1]_2$ $[U_1, Zr_1]_1\langle$fcc_C1$\rangle$, $L[Va_1]_2$ $[U_1, Zr_1]_1\langle$hcp_A3$\rangle$, $L[Va_1]_3$ $[U_1, Zr_1]_1\langle$bcc_A2$\rangle$). Another adjustment would be made only if required by new available information. For the liquid phase, two ternary interaction parameters between metallic and oxide species result from the modelling, $L[U_1, O_2Zr_1]\langle L\rangle$ and $L[O_2U_1, Zr_1]\langle L\rangle$. Due to the nature of the system, and existence of experimental information on the O_2U_1–Zr_1 vertical section, the first parameter is not very influent on the phase diagram and has been fixed to a constant value (50 000 J), denoting a relatively strong immiscibility between the metal and oxide species. Thus, the last ternary interaction parameter, $L[O_2U_1, Zr_1]\langle L\rangle$, appears to be the fundamental one in order to control the extent of the liquid miscibility gap at high temperature, which is a major point of controversy between experimenters, discussed in detail in Section 4.3. Similarly to the O–U binary system, the scarcity and inaccuracy of the difficult experiments in this system at high temperature, has leaded us to propose two extreme cases for this parameter (a: ideal interaction; b: strongly positive interaction).

Finally, the different possibilities for the binary and ternary interaction parameter $L[O_2U_1, U_1]\langle L\rangle$ and $L[O_2U_1, Zr_1]\langle L\rangle$, have been combined to propose two extreme versions of the phase diagram, corresponding to: a: a high oxygen solubility in liquid uranium–zirconium alloys and a small miscibility gap at high temperature; b: a small oxygen solubility and a large liquid miscibility gap.

The optimized Gibbs energy parameters of all condensed phases, i.e. lattice-stabilities, pure metallic and oxide substances, solid solutions and liquid phase, are reported in Appendices A and B and constitute a part of the thermodynamic database for the corium, TDBCR [1].

3. Binary and pseudo-binary sub-systems

3.1. O–U (oxygen–uranium)

3.1.1. Short presentation of the different phases

The phase diagram of the O–U binary system was successively reported in a compilation work by Levin et al. [8–10] and Roth et al. [11]. The condensed solutions and stoichiometric substances, with the symbols currently used in this work, are the following: liquid phase, L; $UO_{2\pm x}$ solid solution, fcc_C1; U_4O_{9-y}, O_9U_4(S); U_3O_{8-x}, O_8U_3(S); UO_3, O_3U_1(S); $U_5O_{13\pm x}$, $O_{13}U_5$(S); U_8O_{21}, $O_{21}U_8$(S); $UO_{2.61}$, $O_{2.61}U_1$(S); α-U, U_1(ort_A20); β-U, U_1(tet); γ-U, U_1(bcc_A2).

3.1.2. Experimental information

3.1.2.1. Phase diagram. In the following, T is the temperature in Kelvin, x(O) the atomic fraction of oxygen in

Table 1
Experimental liquidus of the O–U (U–UO_2) system from Blum et al. [12]

T^L (K)	x^L (O)	x^L (UO_2)
2553	0.543	0.5941
2233	0.439	0.3913
1953	0.315	0.2299
1803	0.233	0.1519

Table 2
Experimental solidus of the O–U (U–UO_2) system from Bates [14]

T^S (K)	x^S (O)	x^S (UO_2)
2673	0.6403	0.89
2473	0.6480	0.9205
2273	0.6525	0.9389
2073	0.6584	0.9637

the O–U system, $x(UO_2)$ the mole fraction of UO_2 in the U–UO_2 system, O/U the oxygen/uranium atomic ratio, L the liquidus or the liquid, and S the solidus or the solid.

Blum et al. [12] have determined the liquidus by using the saturation method (equilibration of U with UO_2 crucibles with subsequent determination of the UO_2 precipitated from the liquid solution) and the solidus by differential thermal analysis. The phase diagram is of eutectic type deported on the uranium rich side ($T = 1403$ K) and the congruent dioxide melting point is extrapolated to about 3063 K. These experimental liquidus temperatures and compositions, corresponding to very large solubilities, have been numerically given by Shunk [13], and are reported in Table 1 as follows.

The homogeneity range of UO_2 extends to hypostoichiometric compositions for low equilibrium O_2 partial pressures. Bates [14] determined the solidus by micrographic observations. The numerical values tabulated by Shunk [13] are reported in Table 2.

The partial uranium–uranium dioxide phase diagram is reported by Elliott [15] as a dashed curve: the solid solubility of O in α-U at 898 K is about $x^{\alpha\text{-U}}(O) = 1 \times 10^{-4}$, $x^{\alpha\text{-U}}(UO_2) = 0.5 \times 10^{-4}$, the one in β-U increases from about $x^{\beta\text{-U}}(O) = 2 \times 10^{-4}$, $x^{\beta\text{-U}}(UO_2) = 1 \times 10^{-4}$ at 898 K to about $x^{\beta\text{-U}}(O) = 3.4 \times 10^{-4}$, $x^{\beta\text{-U}}(UO_2) = 1.7 \times 10^{-4}$ at 948 K, and the one O in γ-U is about $x^{\gamma\text{-U}}(O) = 4 \times 10^{-4}$, $x^{\gamma\text{-U}}(UO_2) = 2 \times 10^{-4}$ from 948 K to 1333 K.

Martin and Edwards [16] showed the existence of a liquid miscibility gap by the metallographic examination of arc-melted alloys. The monotectic was located at $T = 2773 \pm 30$ K, $x^L(UO_2) = 0.65 \pm 0.05$, $x^L(O) = 0.565$, $O/U = 1.30 \pm 0.10$. The liquidus and solidus data, i.e., the hypostoichiometric boundary of urania, were obtained from experiments in which uranium melts were equilibrated with uranium dioxide crucibles in a purified helium atmosphere and then cooled rapidly to room temperature, and from the analyses of the uranium oxide growths. The experimental data are reported from the original figure as follows in Table 3.

Bates [17] determined the melting points for hypostoichiometric UO_{2-x} (2–1.67) in an electric furnace with purified inert atmospheres by microscopy and optical brightness pyrometry, and the original tabulated data are reported in Table 4.

Guinet et al. [18] re-determined the liquidus of the uranium–uranium dioxide system above 1403 K (eutectic temperature) by the saturation method (see Ref. [12]) and the solidus by differential thermal analysis. The monotectic was located at 2743 ± 30 K, and its composition was established by micrographic and chemical analysis, $x^L(UO_2) = 0.59$, $x^L(O) = 0.541$, $O/U = 1.18$. The phase diagram is an eutectic type deported on the uranium rich side and the liquid miscibility gap extends from $x^L(UO_2) = 0.47$–0.59, $x^L(O) = 0.484$–0.541. The compositions of the liquid and solid issued from the decomposition of the monotectic liquid result from the extrapolation of the liquidus and solidus data obtained at lower temperature. The hypostoichiometric compound UO_{2-x} shows a minimum O/U ratio equal to 1.6, $x^S(O) = 0.6154$, $x^S(UO_2) = 0.8$, at the monotectic temperature. The composition of the solid UO_{2-x} compound at the monotectic temperature is reported from

Table 3
Experimental liquidus and solidus of the O–U (U–UO_2) system from Martin and Edwards [16]

T^LK	x^L (O)	x^L (UO_2)	T^S (K)	x^S (O)	x^S (UO_2)
2773	0.0485	0.0255	2773	0.6227	0.8254
2673	0.0215	0.011	2702	0.6227	0.8254
2673	0.0472	0.0248	2591	0.626	0.8372
2573	0.0128	0.0065	2531	0.634	0.8661
2493	0.0142	0.0072	2473	0.639	0.8853
2273	0.006	0.003	2373	0.648	0.9223
2173	0.0036	0.0018	2273	0.6506	0.9312
			2191	0.653	0.9410
			2096	0.658	0.9623
			1873	0.6628	0.9830

Table 4
Experimental liquidus of the O–U (U–UO_2) system from Bates [17]

T^L (K)	O/U	X^L (O)	X^L (UO_2)
3063 ± 17	2.002	0.6669	1.001
3077 ± 13	2.001	0.6668	1.0005
3065 ± 9	1.922	0.6578	0.961
3008 ± 25	1.917	0.6572	0.9585
3017 ± 19	1.889	0.6538	0.9445
2976 ± 22	1.878	0.6525	0.939
2989 ± 28	1.871	0.6517	0.9355
3019 ± 8	1.868	0.6513	0.934
2974 ± 21	1.841	0.6480	0.9205
2994 ± 12	1.823	0.6458	0.9115
2954 ± 8	1.803	0.6432	0.9015
2971 ± 17	1.794	0.6421	0.897
2900 ± 22	1.792	0.6418	0.896
2876 ± 17	1.780	0.6403	0.89
2937 ± 25	1.778	0.64	0.889
2921 ± 24	1.735	0.6344	0.8675
2841 ± 27	1.713	0.6314	0.8565
2806 ± 31	1.686	0.6277	0.848

micrographic analysis as $x^S(UO_2)$, O/U, $x^S(O) = 0.797$, 1.594, 0.6145; 0.806, 1.612, 0.6172; 0.818, 1.636, 0.6206. The experimental data taken from a figure are reported in Table 5.

Bannister [19] measured both solidus and liquidus temperatures on the UO_2 rich side. The monotectic was located at 2693 ± 70 K, with $(O/U)^S = 1.62 \pm 0.06$, $x^S(O) = 0.618$, $x^S(UO_2) = 0.81$. The melting point of UO_2 is located at 3133 ± 70 K. According to the author in its original paper, the most reliable value appears to be 3078 ± 15 K. The experimental data (±70 K) taken from a figure are reported in Table 6.

Ackermann et al. [20] determined the lower phase boundary of the hypostoichiometric compound UO_{2-x} by an isopiestic method from 1900 to 2500 K. Data taken from a figure are reported in Table 7.

Latta and Fryxell [21] determined solidus and liquidus temperatures for urania to ±15 K over the composition range $UO_{1.5}$–$UO_{2.23}$. The congruent composition is UO_2, 3138 K, and the monotectic composition is $UO_{1.46}$, 2698 K, $x^L(O) = 0.593$, $x^L(UO_2) = 0.73$. Data were obtained by a thermal arrest technique, using samples sealed in tungsten or rhenium. The liquidus and solidus data are taken from the original table and reported in Table 8.

A great discrepancy is observed concerning the solubility of O in liquid uranium versus temperature measured by Martin and Edwards [16] and Guinet et al. [18], who explained in detail the encountered experimental difficulties: *they are mainly due to the existence of a thermal gradient between the crucible and the bath... Only a cooling which maintains the homogeneity of temperature in the liquid allows to precipitate the molten dioxide in its mass*. According to Garg and Ackermann [22], *the difference is mainly due to the different methods employed for quenching and sampling*, and that is why they used a simple method, developed by Ackermann and Rauh [23] and Garg and Ackermann [24], which does not involve post-experimental evaluation of the quenched sample: the solubility of oxygen in liquid uranium and the composition of the lower phase boundary of uranium dioxide at 1950 K has been determined as $x^L(UO_2) = 0.0298 \pm 0.008$, $x^L(O) = 0.056$, and $x^S(UO_2) = 0.9746 \pm 0.003$, $x^S(O) = 0.6609$.

In a thermochemical study, Wang and Olander [25] selected this point associated to a similar temperature dependence than Guinet et al. [18]. The calculated liquidus taken from a figure is reported as follows in Table 9.

Kotlar et al. [26] determined the phase boundaries of the O–U system by oxygen transport in the domain $2.19 < O/U < 2.63$ and $1353\ K < T < 1473\ K$.

Matsui and Naito [27] studied the phase relation and defect structures of non-stoichiometric $U_4O_{9\pm y}$ and UO_{2+x} at high temperatures. Phase relations in the composition range UO_{2+x} to U_3O_{8-z} were determined by electrical-conductivity measurements and X-ray diffraction in the ranges $1298\ K < T < 1413\ K$ and 10^{-7} atm $< P_{O_2}$ 10^{-3} atm. The peritectoid reaction $U_4O_{9\pm y} \leftrightarrow UO_{2+x} + U_3O_{8-z}$ was estimated to be present between 1399 K and 1404 K.

Caneiro and Abriata [28] determined the equilibrium partial pressure of oxygen in the uranium-oxygen system

Table 5
Experimental liquidus and solidus of the O–U (U–UO_2) system from Guinet et al. [18]

T^L (K)	X^L (O)	X^L (UO_2)	T^S (K)	X^S (O)	X^S (UO_2)
1803	0.107	0.06	2223	0.6479	0.92
2003	0.1212	0.08	2443	0.6364	0.875
2133	0.2089	0.132	2493	0.635	0.87
2223	0.2401	0.158	2573	0.631	0.855
2293	0.27	0.185			
2433	0.29	0.204			
2503	0.342	0.26			
2573	0.3976	0.33			

Table 6
Experimental liquidus and solidus of the O–U (U–UO_2) system from Bannister [19]

T^L (K)	O/U	x^L (UO_2)	x^L (O)	T^S (K)	O/U	x^S (UO_2)	x^S (O)
2993	1.808	0.9041	0.644	2963	1.847	0.9336	0.649
2933	1.749	0.8746	0.636	2893	1.808	0.9041	0.644
2798	1.604	0.8023	0.616	2823	1.749	0.8746	0.636
2753	1.585	0.7925	0.613	2753	1.685	0.8425	0.628
2693	1.528	0.7639	0.604	2693	1.607	0.8033	0.616

by a thermogravimetric technique in the composition range $2.61 < O/U < 2.67$ and temperatures between 800 K and 1400 K. The nearly stoichiometric phase $U_3O_{8\pm z}$ has been confirmed to exist in the U–O system, together with a non-stoichiometric $U_8O_{21\pm x}$ phase which is stable in the range $2.617 < O/U < 2.655$; the high precision of the experimental setup has permitted the determination of the narrow two phase region $U_3O_{8\pm z}$ + $U_8O_{21\pm x}$ with small errors. The partial molar enthalpy and entropy of solution of oxygen in the $U_8O_{21\pm x}$ phase have also been evaluated.

3.1.2.2. Thermodynamics. Saito [29] measured the thermodynamic properties of uranium oxides with O/U atomic ratios between 2.04 and 2.34, principally in the nonstoichiometric UO_{2+x} single-phase region, at temperatures in the range 773–1373 K by electromotive force measurements with cells of the type Ni–NiO / ZrO_2 (+CaO). The relative partial molar free energies of oxygen for the single-phase region UO_{2+x} and the two-phase coexisting regions UO_{2+x}–U_4O_{9-y} and U_4O_9–U_3O_{8-z} were obtained with adequate precision.

Marchidan and Matei Tanasescu [30–33] obtained the thermodynamic data for some uranium oxides with non-stoichiometric compositions by electromotive force measurements on high-temperature galvanic cells containing solid electrolyte. They calculated the partial molar free energies, enthalpies and entropies of solution of oxygen in uranium oxides and the corresponding relative integral quantities as a function of temperature, as well as the equilibrium pressures of oxygen over the two oxides (1073–1373 K, $UO_{2.18}$, $UO_{2.20}$, $UO_{2.26}$, $UO_{2.28}$, $UO_{2.30}$, $UO_{2.50}$, U_4O_9 + U_3O_8).

Javed [34] performed transpiration experiments in the temperature range 1873–2173 K to study the thermodynamics of hypostoichiometric urania and established the oxygen partial pressures by using flowing H_2/H_2O mixtures. After equilibration the quenched products were analysed by chemical, X-ray and metallographic techniques. The results were plotted as ΔG_{O_2} versus the O/U ratios (1.96–2) for various temperatures.

Table 7
Experimental solidus of the O–U (U–UO_2) system from Ackermann et al. [20]

T^S (K)	x^S (UO_2)	x^S (O)
1873	0.98	0.662
2020	0.965	0.659
2101	0.960	0.658
2192	0.940	0.653
2243	0.936	0.652
2339	0.915	0.647
2418	0.888	0.64
2479	0.875	0.636
2501	0.865	0.634
2521	0.846	0.628

Table 8
Experimental liquidus and solidus of the O–U (U–UO_2) system from Guinet et al. [18]

O/U	x (UO_2)	x (O)	T^L (K)	T^S (K)
2.23	1.115	0.6904	2837	3031
2.23	1.115	0.6904	2851	3013
2.184	1.092	0.6859	2878	3045
2.13	1.065	0.6805	2940	3078
2.12	1.06	0.6795	2907	3071
2.095	1.0475	0.6769	3003	3088
2.095	1.0475	0.6769	3001	3090
2.095	1.0475	0.6795	3067	3109
2.058	1.029	0.673	3085	3136
2.022	1.011	0.669	3109	3125
2.019	1.0095	0.6688	3118	3138
1.998	0.999	0.6664	3118	3138
1.997	0.9985	0.6663	3120	3135
1.997	0.9985	0.6663	3107	3133
1.993	0.9965	0.6659	3105	3133
1.980	0.99	0.6644	3106	3133
1.956	0.978	0.6617	3076	3130
1.943	0.9715	0.6602	3069	3118
1.920	0.96	0.6575	3043	3113
1.890	0.945	0.654	3002	3105
1.856	0.928	0.65	2970	3083
1.809	0.9045	0.644	2888	3033
1.803	0.9015	0.643	2893	3033
1.793	0.8965	0.642	2874	3031
1.750	0.875	0.636	2818	2983
1.790	0.895	0.642	2763	3013
1.736	0.868	0.634	2786	2968
1.662	0.831	0.624	2686	2923
1.600	0.8	0.615	2696	2857
1.556	0.778	0.609	2708	2783
1.500	0.75	0.6	2701	2771

Table 9
Calculated liquidus of the O–U (U–UO_2) system from Wang and Olander [25]

T^L (K)	O/U	x (UO_2)	x (O)
2673	0.303	0.131	0.232
2473	0.215	0.097	0.177
2273	0.14	0.065	0.123
2073	0.0827	0.040	0.076
1873	0.05	0.024	0.048

Wheeler [35] measured equilibrium oxygen potentials for UO_{2-x} in the temperature range 1800–2000 K and O/U ratio = 1.98–2 by using a technique in which the UO_{2-x} sample was equilibrated in an oxygen potential controlled by the equilibrium $2C + O_2 \leftrightarrow 2CO$.

Picard and Gerdanian [36] used the microcalorimetric method for determining the partial molar enthalpy ΔH_{O_2} in uranium oxides between $UO_{2.00}$ and $UO_{2.60}$. The obtained boundaries for the domains UO_{2+x} and U_4O_{9-y} are in perfect agreement with those determined by Kotlar et al. [26]. The thermodynamic quantities for the U_4O_{9-y} oxides as well as the standard formation enthalpy at 1323 K of $UO_{2.2413}$ were calculated.

Aronson and Belle [37] made a thermodynamic study of the uranium-oxygen system, primarily in the single phase region $UO_{2.00}$–$UO_{2.20}$ at temperatures of 1150–1350 K (O/U = 2.013–2.505). An electrochemical technique was used to obtain EMF measurements on uranium oxide half-cells. Partial molar free energies, entropies and enthalpies of solution of oxygen in UO_{2+x} were calculated.

Tetenbaum and Hunt [38] measured the total pressure of uranium-bearing species over bivariant oxygen-deficient urania compositions in the temperature range 2080–2705 K, using the transpiration method with flowing H_2–H_2O mixtures.

Lindemer and Besmann [39] made a chemical thermodynamic representation of $UO_{2\pm x}$. The entire $UO_{2\pm x}$ database for the dependence of non-stoichiometry, x, on temperature and chemical potential of oxygen was retrieved from the literature and represented. This database was interpreted by least-squares analysis using equations derived from the classical theory for the solid solution of a solute in solvent.

3.1.3. Optimization results

3.1.3.1. Numerical data. The Gibbs energy parameters of pure oxide UO_2(fcc_C1, L) have been calculated from the selected fundamental thermodynamic values assessed separately [2]. For the compounds UO_3(S), U_3O_8(S) and U_4O_9(S), the fundamental thermodynamic values are based on the compilation work of Cordfunke et al. [40]. The heat capacity has been directly taken, while the enthalpy of formation and entropy at room temperature have been slightly modified in order to be consistent with the phase diagram.

The main solutions of the O-U binary system are the liquid phase and the fcc_C1 solid solution, $UO_{2\pm x}$, which exists over the composition range $UO_{1.67}$–$UO_{2.27}$. The other compounds above the atomic ratio O/U equal to 2 may present a narrow homogeneity range, and thus will be considered as stoichiometric in this study.

Most of the experimental phase diagram information concerns the UO_2–U region. For that reason, we have first optimized this part of the O–U system and then extended the model to the entire system. The liquid phase, L, has been represented by means of a non-ideal associate model, using the formula $[O_1, O_2U_1, U_1]\langle L\rangle$. The interaction parameter between O_2U_1 and U_1 has been optimized by using the experimental information below the atomic ratio O/U = 2. The interaction between O and O_2U_1 has been optimized by using the experimental information above the atomic ratio O/U = 2. Due to the very negative value of the Gibbs energy of O_2U_1, the interaction between O and U can be neglected. In order to permit the deviation from the ideal stoichiometry O_2U_1 of the compound $UO_{2\pm x}$, the fcc_C1 solid solution has been described by a two-sublattice model, in which vacancies, Va, are present on each sublattice, with the formula $[O_1, Va]_2[U_1, Va]_1\langle fcc\_C1\rangle$. It does not mean that it represents the real structure of this phase, but it allows to describe satisfactorily both the phase diagram and the oxygen potential. The interaction parameters have been optimized from solubility limits and thermodynamics information.

Due to the controversy between experimenters about the solubility of oxygen in liquid uranium and its consequences on the extent of the liquid miscibility gap at high temperature, two different optimizations have been performed, leading to two different sets of parameters for the interaction term $L[O_2U_1, U_1]\langle L\rangle$ and two different versions of the phase diagram.

The first set of parameters (a) is more naturally obtained from the whole experimental information, but we have taken a higher weight to the experimental point of Garg and Ackermann [22] in the optimization procedure, because they have given explanations to the experimental difficulties encountered by other authors.

The second set of parameters (b) has been obtained by imposing a small solubility of oxygen similar to the one determined by Martin and Edwards [16].

The whole experimental information concerning thermodynamics has been taken into account, except thermodynamic data of Pattoret [41].

3.1.3.2. Graphical outputs. The two versions of the calculated phase diagram by using the two different sets of parameters compared to the available experimental information is presented on Fig. 1(a) and (b). For the version (a), the calculated oxygen solubility in liquid uranium on the uranium–uranium dioxide side, is very near the one measured by Garg and Ackermann [22] and

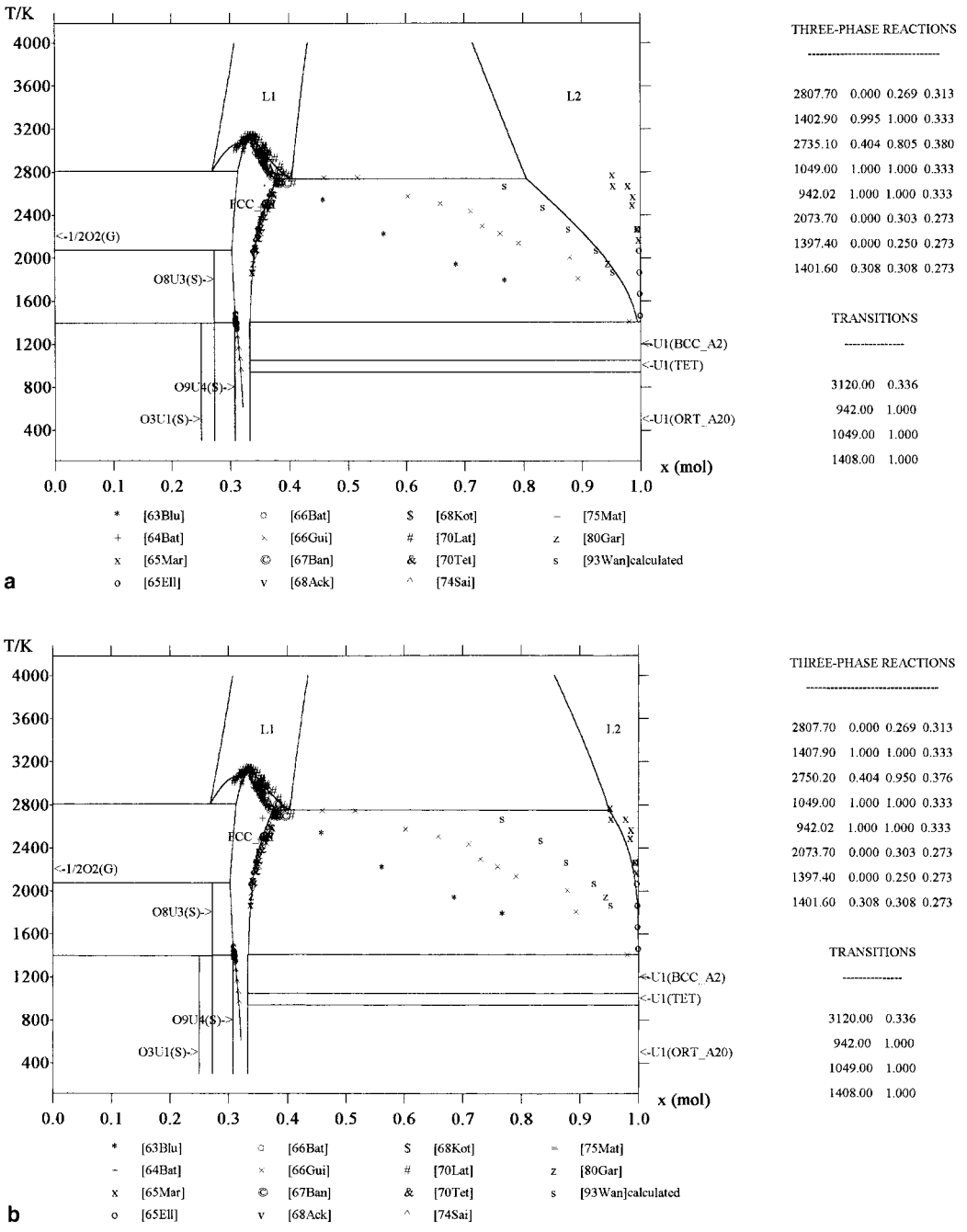

Fig. 1. (a) Calculated O–U equilibrium phase diagram compared to the experimental information (with the hypothesis of a large oxygen solubility in liquid uranium). (b) Calculated O–U equilibrium phase diagram compared to the experimental information (with the hypothesis of a small oxygen solubility in liquid uranium).

lies between the one determined by Martin and Edwards [16] and Guinet et al. [18]. For the version (b), the oxygen solubility is in agreement with the experimental data of Martin and Edwards [16].

The monotectic reaction L1↔fcc_C1 + L2 is calculated as: (a) $T = 2735.10$ K, $x^{L1}(O) = 0.596$, $x^{fcc\_C1}(O) = 0.62$, $x^{L2}(O) = 0.195$; (b) $T = 2750.20$ K, $x^{L1}(O) = 0.596$, $x^{fcc\_C1}(O) = 0.624$, $x^{L2}(O) = 0.05$.

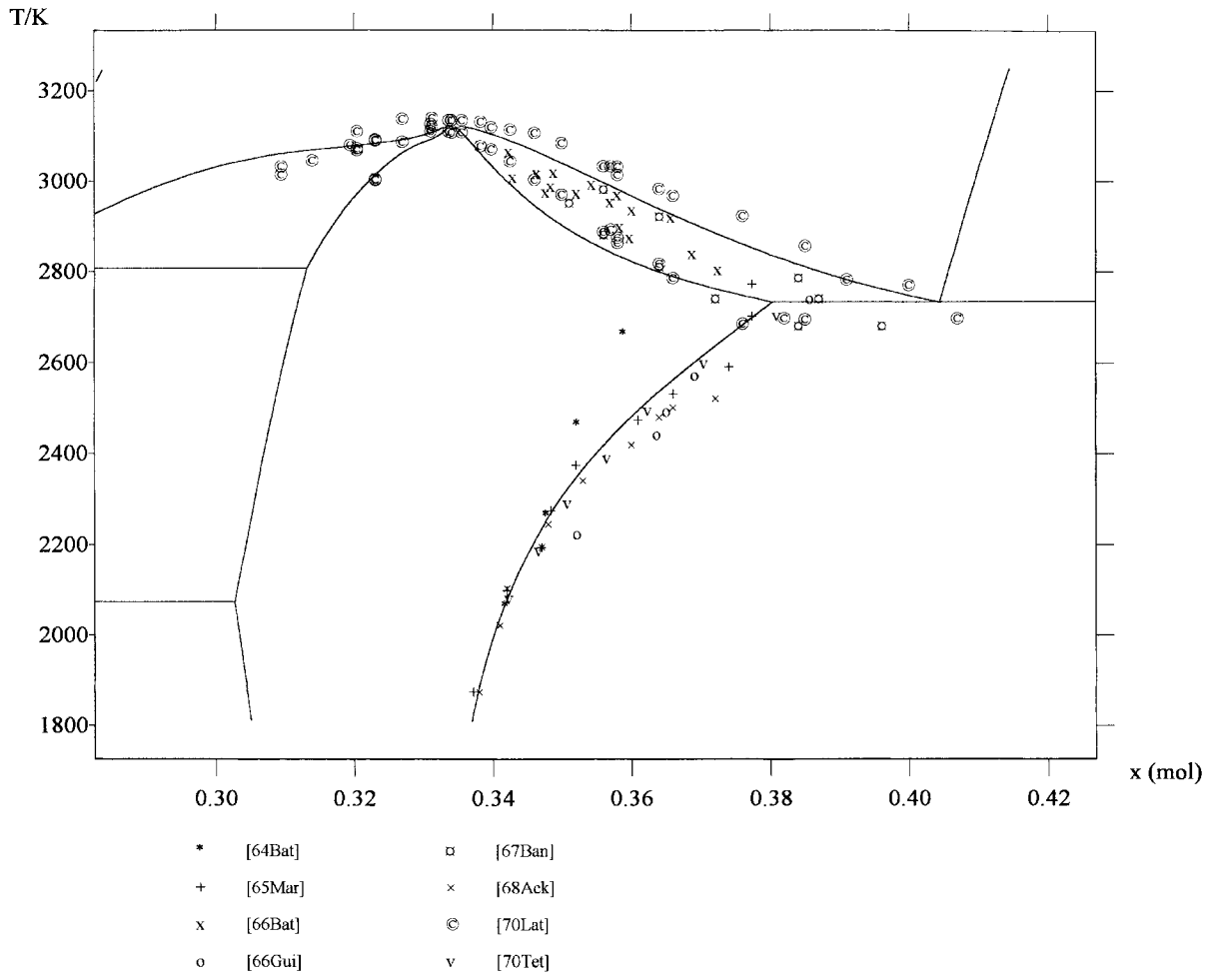

Fig. 2. Calculated $UO_{2\pm x}$ region compared to the experimental information.

These values have to be compared to the experimental from Martin and Edwards [16], $T = 2773 \pm 30$ K, $x^{L1}(O) = 0.565$ and Guinet et al. [18], $T = 2743$ K $\pm$ 30 K, $x^{L1}(O) = 0.541$, $x^{fcc\_C1}(O) = 0.617$.

An enlargement of the $UO_{2\pm x}$ region is presented in Fig. 2. The liquidus at high temperature in the O_2U_1 rich part is satisfactorily represented, as well in the hypostoichiometric as in the hyperstoichiometric region. The agreement between the calculated solubilities of oxygen and uranium in solid UO_2 (solidus) and the experimental information is very satisfactory.

The calculated oxygen potential in $UO_{2\pm x}$ has been compared to the experimental one of various authors at different temperatures for both hyperstoichiometric [29–33,36,37] and hypostoichiometric [34,35] compositions and the agreement is quite satisfactory. Examples of comparison in the over-stoichiometry and sub-stoichiometry regions are presented in Figs. 3 and 4.

3.2. O–Zr (oxygen–zirconium)

3.2.1. Short presentation of the different phases

The phase diagram of the Zr-ZrO_2 system has been reported by Hansen and Anderko [42] in agreement with Domagala and McPherson studies [43], and reinvestigated by Ackermann et al. [44]. The experimental information has been compiled by Abriata et al. [45]. The condensed solutions and stoichiometric substances, with the symbols currently used in this work, are the following: liquid phase, L; ZrO_{2-x} solid solution, fcc_C1, cubic; ZrO_2(tet), tetragonal; ZrO_2(mon), monoclinic; α-Zr, hcp_A3; β-Zr, bcc_A2.

3.2.2. Experimental information

3.2.2.1. Phase diagram. Domagala and McPherson [43] determined the constitution of the system Zr–ZrO_2. Iodide zirconium was combined with calculated amounts

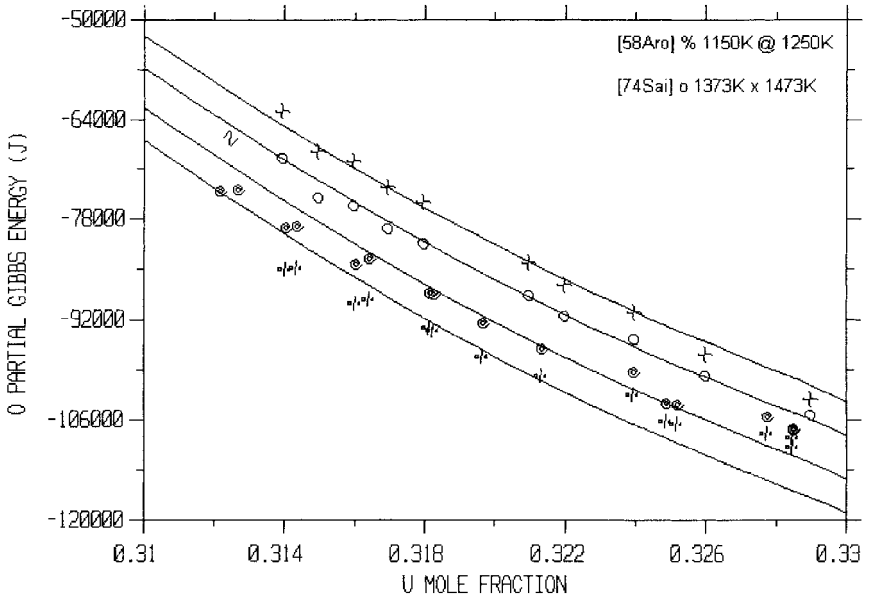

Fig. 3. Calculated oxygen potential in UO_{2+x} region compared to the experimental one.

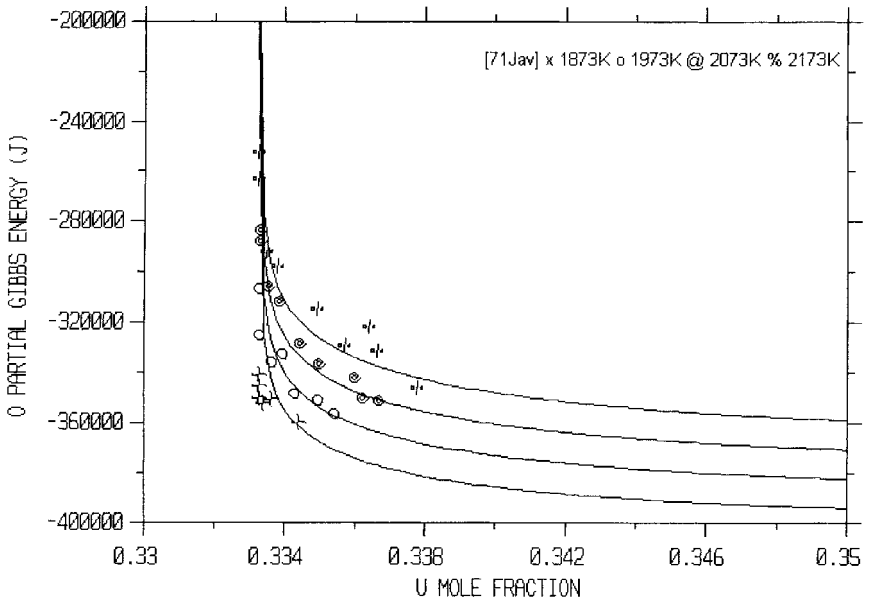

Fig. 4. Calculated oxygen potential in UO_{2-x} region to the experimental one.

of ZrO_2 or master alloys and arc-melted. Annealing treatments were carried out at 21 temperatures levels. Metallographic examination of the heat treated specimens permitted construction of the binary phase diagram from zirconium to ZrO_2. Oxygen additions to zirconium raise the transformation temperature as well as the melting point. Features of the diagram include the peritectic formation of β, the transformation of α directly from the melt, an intermediate phase ZrO_2 with a range of homogeneity, and an eutectic between α and ZrO_2. The following invariant reactions are reported: L + α ↔ β at $T = 2213$ K, $x^{L}(Zr) = 0.933$, $x^{\alpha}(Zr) = 0.818$, $x^{\beta}(Zr) = 0.896$; L ↔ α + ZrO_2(fcc_C1) at $T = 2173$ K, $x^{L}(Zr) = 0.59$, $x^{\alpha}(Zr) = 0.708$, $x^{fcc\_C1}(Zr) = 0.37$; L ↔ α at $T = 2248$ K, $x^{\alpha,\,L}(Zr) = 0.75$; L↔$ZrO_2$(fcc_C1) at $T = 2973$ K; ZrO_2(tet) ↔ α + ZrO_2(mon) at about

1273 K. The experimental data taken from the original figure are reported in Table 10.

Holmberg and Magneli [46] and Holmberg and Dagerhamn [47] found the solubility limit of oxygen in α-Zr equal to 28.6 at.% O ($ZrO_{0.40}$) in the temperature region 673–1073 K by X-ray methods.

Gebhardt et al. [48] established the constitution of the Zr–ZrO_2 system by means of metallographic investigation and resistivity measurements. The phase diagram differs from earlier diagrams referred to solubility of oxygen in α-Zr, the delineation of the two phase region between α and β zirconium, and the solubility limit of Zr in ZrO_2. The form of this last suggests the existence of a high temperature form of ZrO_2 stable above 1850 K, which could not be retained by quenching and was therefore not investigated further. Numerical data are reported in Table 11.

Ruh and Garrett [49] studied the nonstoichiometry of ZrO_2 and its relation to tetragonal-cubic inversion in ZrO_2. The system Zr–O was studied in the composition range 50–66.7 at.% O by metallographic analysis, high-temperature X-ray analysis, and lattice parameter determinations at room temperature. The solubility of zirconium in zirconia was determined from 1473–2273 K and the tetragonal-cubic inversion of ZrO_2 was shown to be lowered to approximately 1763 K for samples containing α-Zr and oxide phase. α zirconium has greater solubility in the cubic phase than in the tetragonal phase, and the inversion is revealed, in samples quenched from the cubic field, by the exsolution of α-Zr, which is metallographically characterized as striations. The invariant reaction $ZrO_2(fcc\_C1) \leftrightarrow \alpha + ZrO_2(tet)$ was located at about 1763 K, $x^{fcc\_C1}(Zr) = 0.37$, $x^{tet}(Zr) = 0.35$.

Table 10
Experimental phase diagram of the O–Zr system from Domagala and McPherson [43]

T (K)	wt% (O)	wt% (O)	x (Zr)	x (Zr)
	β/β + α	β + α/α	β/β + α	β + α/α
1173	0.10	0.65	0.99432	0.96404
1223	0.15	1.09	0.99151	0.94088
1273	0.20	1.38	0.98870	0.92611
1373	0.35	1.84	0.98037	0.90344
1473	0.65	2.18	0.96404	0.88726
1573	0.85	2.52	0.95340	0.87154
1673	1.00	2.75	0.94554	0.86116
1773	1.25	2.98	0.93268	0.85097
1873	1.43	3.21	0.92360	0.84098
1973	1.61	3.38	0.91466	0.83371
2073	1.78	3.56	0.90635	0.82612
2123	1.89	3.67	0.90103	0.82154
2213	2.00	3.75	0.89577	0.81823
	α/α + ZrO_2	α + ZrO_2/ZrO_2	α/α + ZrO_2	α + ZrO_2/ZrO_2
973	6.75	24.88	0.70785	0.34621
1173	–	24.67	–	0.34876
1273	–	24.44	–	0.35159
1473	–	24.22	–	0.35432
1673	–	24.00	–	0.35707
1773	–	23.78	–	0.35986
1873	–	23.56	–	0.36267
1973	–	23.33	–	0.36563
2073	–	23.20	–	0.36732
2173	6.75	23.00	–	0.36994
	β/L + β	L + β/L	β/L + β	L + β/L
2128	1.00	0.09	0.94554	0.99489
2193	1.84	1.00	0.90344	0.94554
2213	2.00	1.25	0.89577	0.93268
	L/L + ZrO_2	L + ZrO_2/ZrO_2	L/L + ZrO_2	L + ZrO_2/ZrO_2
2173	11.0	23.0	0.58661	0.36994
2273	12.3	23.3	0.55566	0.36602
	α/L + α	L + α/L	α/L + α	L + α/L
2248	5.28	5.28	0.75882	0.75882

Table 11
Experimental phase diagram of the O–Zr system from Gebhardt et al. [48]

T (K)	at.% (O)			
	β/β + α	β + α/α	α/α + ZrO_2	α + ZrO_2/ZrO_2
1530	4.0			66.5
1580			30.4, 28.5	
1630	5.9		30.7, 30.5	
1730	7.0	15.0	31.2, 31.2	66.5
1830	8.2	16.5	30.5, 30.4	63.5
1930	10.0	17.5	31.7, 31.7	63.2
2030	11.1	18.2	32.5	63.0

Ackermann et al. [44] investigated the high-temperature phase diagram for the system Zr–O. The melting, eutectic, peritectic, solidus and liquidus temperatures have been measured directly by a simple optical pyrometric technique requiring only a few hundred milligrams of sample. The saturation solubility of oxygen in α-Zr between 1543 K and 2253 K, and the lower phase boundary of the ZrO_{2-x} phase between 2173 K and 2673 K have been measured by an isopiestic equilibration method. The oxygen solubility limit in α-Zr agrees well with previous low-temperature studies and reaches a maximum solubility of 35 ± 1 at.% O at the eutectic temperature, 2338 ± 5 K. The maximum melting temperature of α-Zr is 2403 ± 10 K and corresponds to a composition of 25 ± 1 at.% O. Both of these temperatures are approximately 150 K higher than previously reported. Liquidus compositions above the eutectic temperature were obtained via mass spectrometry from the kinetic behavior of the liquid solution–ZrO_{2-x} mixture as it approached equilibrium at 2398 ± 5 K. The lower phase boundary or solidus of the ZrO_{2-x} phase departs appreciably from ideal stoichiometry above 2173 K and smoothly reaches its most reduced composition, 61 at.% O($ZrO_{1.56}$) near 2573 K. The solidus is retrograde at higher temperatures. The melting temperature of the stoichiometric dioxide is 2983 ± 15 K. In summary, the following invariant reactions are reported: L + α ↔ β at $T = 2243$ K, $x^{\alpha}(Zr) = 0.81$, $x^{\beta}(Zr) = 0.89$; L ↔ α + ZrO_2(fcc_C1) at $T = 2338$ K, $x^{L}(Zr) = 0.60$, $x^{\alpha}(Zr) = 0.65$, $x^{fcc\_C1}(Zr) = 0.38$; L ↔ α at $T = 2403$ K, $x^{\alpha, L}(Zr) = 0.75$; L ↔ ZrO_2(fcc_C1) at $T = 2983$ K. Numerical data are reported in Table 12.

Ackermann et al. [50] determined the composition of the lower phase boundary of the substoichiometric dioxide, ZrO_{2-x}, from 2229–2677 K by vapor phase equilibration. These results appeared to be in near agreement with those reported at T < 2033 K by Gebhardt et al. [48], although they appeared to be somewhat more reduced. Therefore, the equilibration measurements have been extended to lower temperatures (2088–2318 K) to ascertain any real discrepancy and to examine the lower phase boundary of ZrO_{2-x} for as low a temperature as is practical. This region of the phase diagram is, therefore, more fully described from all presently available evidence. Numerical data are reported in Table 13.

Tanabe et al. [51] have made AES and XPS studies of oxygen stabilized α-Zr(O) with various oxygen contents in order to examine the effect of oxygen on AES and XPS spectra of zirconium. At 1400 K, one phase was

Table 12
Experimental phase diagram of the O–Zr system from Ackermann et al. [44]

at.% (Zr)					
T (K)	α/α + ZrO_2	T (K)	ZrO_2/α + ZrO_2	T (K)	L/L + ZrO_2
1546	70.2	2229	36.5	2401	58
2089	67.1	2282	37.2	2396	58.8
2158	66.6	2328	37.6	2401	59.7
2253	66.3			2392	58
T (K)	ZrO_2/L + ZrO_2	T (K)	L/L + α	T (K)	α/L + α
2364	37.8	2254	89.3	2338	65
2417	38.4	2297	88.0	2360	67
2475	38.7	2393	76.9	2403	75
2517	38.9	2403	76.0	2243	80.5
2525	38.9	2381	67.0		
2586	39.2	2338	60.0		
2650	38.6				
2677	38.4				
T (K)	L/L + β	T (K)	β/L + β		
2234	93.7	2243	89.5		
		2241	90.6		
		2191	92.7		
		2145	95.2		

observed at 25 at.% O (α-Zr) and two phases at 30 at.% O (α-Zr + ZrO_2).

3.2.2.2. Thermodynamics. Kornilov et al. [52] determined the relationship $\Delta H^{\circ}_{f,298.15\ K}(ZrO_x) = -(585.3416 \pm 10.46\ kJ)x$ for the α phase by heats of combustion measurements of three preparations if ZrO_x: $ZrO_{0.079\pm0.005}$, −41.84 ± 2.5104; $ZrO_{0.201\pm0.005}$, −119.244 ± 2.5104; $ZrO_{0.333\pm0.005}$, −194.556 ± 2.5104 kJ/g atom Zr.

Wang and Olander [25] have used the thermodynamic constraints relating the standard free energy of formation of an oxide MOc to its oxygen potential to develop the full spectrum of oxygen potentials of the U–O and Zr–O system. Contrarily to the U–O system, oxygen potential information for the Zr–O system is scant and far less consistent. Oxygen pressure in the oxygen-containing metal regions where no data are available have been estimated and compared to our calculated results in Table 14.

The vaporization behavior of the univariant system Zr(S, L) + ZrO_2(S) has been investigated by a combination of mass effusion and mass-spectrometric techniques over the temperature range 1890–2500 K by Ackermann et al. [55]. The partial pressures of the gaseous species and the activity and activity coefficient of Zr and ZrO_2 in the condensed phases have been determined. The activity of zirconium is reported from the original figure in Table 15.

Rauh and Garg [56] used similar technique for the sub-stoichiometric dioxide in the range 1850–2860 K. The partial pressures were also determined, and the standard Gibbs energies of formation of the sub-stoichiometric dioxide were deduced as functions of temperature and compositions.

Boureau and Gerdanian [53,54] have determined the partial molar enthalpy of mixing of oxygen in zirconium and hafnium by the Tian–Calvet microcalorimetric method at 1323 and 1573 K.

3.2.3. Optimization results

3.2.3.1. Numerical data. The Gibbs energy parameters of pure oxide ZrO_2(monoclinic, tetragonal, fcc_C1, L) have been calculated from the selected fundamental thermodynamic values assessed separately [2].

The main solutions of the O–Zr binary system are the liquid phase, the fcc_C1 solid solution (ZrO_{2-x}), because zirconia can exist over the composition range 60.8–66.67 at.% O, $ZrO_{1.55}$–ZrO_2, the bcc_A2 and hcp_A3 terminal zirconium rich solutions. All the experimental phase diagram information concerns the ZrO_2–Zr region. For that reason, we have first optimized this part of the O–Zr system and then extended the model to the entire system. The hyperstoichiometric boundaries of the fcc_C1 solid solution are experimentally unknown and thus, the phase has been limited to ZrO_2. The liquid phase, L, has been represented by means of an associate model, using the formula $[O_1, O_2Zr_1, Zr_1]\langle L\rangle$. The Gibbs energy of the pure reference components has been previously described. The interaction parameter between O_2Zr_1 and Zr_1 has been optimized by using the experimental information below the atomic ratio O/Zr = 2. The interaction between O and O_2Zr_1 has been assumed to be equal to zero because there is no available phase diagram information above the atomic ratio O/Zr = 2. Due to the very negative value of the Gibbs energy of O_2Zr_1, the interaction between O and Zr can be neglected. In order to permit the deviation from the ideal stoichiometry O_2Zr_1 of the compound $ZrO_{2\pm x}$, the

Table 13
Lower phase boundary of ZrO_{2-x} from Ackermann et al. [51]

$ZrO_2/\alpha + ZrO_2$		
T (K)	*O*/Zr	at.% (Zr)
2088	1.706	36.95
2148	1.684	37.26
2218	1.671	37.44
2243	1.686	37.23
2293	1.673	37.41
2318	1.646	37.79

Table 14
Oxygen pressure versus temperature in the hcp_A3(α), $L + ZrO_{2-x}$ region

PO_2(atm)		
T (K)	[25]	This work
1873	10^{-22}	2.0×10^{-21}
1950	10^{-21}	2.9×10^{-20}
2028	10^{-20}	3.6×10^{-19}
2090	10^{-19}	2.3×10^{-18}
2195	10^{-18}	4.2×10^{-17}
2273	10^{-17}	3.1×10^{-16}
2338	10^{-16}	1.4×10^{-15}
2450	10^{-15}	2.0×10^{-14}
2561	10^{-14}	2.5×10^{-13}

Table 15
Activity of Zr in the univariant Zr (S, saturated with O) + $ZrO_{2-x}(S)$ region

a(Zr)		
T (K)	[55]	This work
1800	0.52	0.532
1900	0.57	0.538
2000	0.62	0.544
2100	0.67	0.547
2200	0.72	0.572
2300	0.78	0.604

fcc_C1 solid solution has been described by a two-sublattice model, in which vacancies are present on each sublattice, with the formula $[O_1, Va]_2[Zr_1, Va]_1\langle fcc\_C1\rangle$. It does not mean that it represents the real structure of this phase, but it allows to describe satisfactorily the phase diagram. The Gibbs energy of the pure reference components has been previously described. The interaction parameters have been optimized from solubility limits information, but only on the ZrO_2–Zr part. The hcp_A3 terminal zirconium rich solid solution has been described by a two-sublattice model, with the formula $[O_1, Va]_2[Zr_1]_1\langle hcp\_A3\rangle$. The Gibbs energy of the pure Zr(hcp_A3) has been previously described, while the value for metastable O_2Zr_1(hcp_A3) has been arbitrarily fixed to a high positive value. The interaction parameter has been optimized from the experimental phase diagram and thermodynamic data (enthalpy of formation, activity). The bcc_A2 terminal zirconium rich solid solution has been described by a two-sublattice model, with the formula $[O_1, Va]_3[Zr_1]_1\langle bcc\_A2\rangle$. The Gibbs energy of the pure Zr(bcc_A2) has been previously described, while the value for metastable O_3Zr_1(bcc_A2) has been arbitrarily fixed to a high positive value. The interaction parameter has been optimized from the experimental phase diagram.

The enthalpy of formation $\Delta H^{\circ}_{f,298.15\ K}$ (α-Zr) has been optimized by using the experimental data of Kornilov et al. [53]. The calculated partial pressure of oxygen has been compared to the estimated values of Wang and Olander [25] in Table 14, and the activity of zirconium to the experimental one of Ackermann et al. [55] in Table 15. The agreement is reasonable according to the uncertainties of the compared data.

3.2.3.2. Graphical outputs. The calculated phase diagram compared to the available experimental information is presented in Fig. 5.

The agreement between the calculated phase diagram and the available experimental information is quite satisfactory. However, there is a lack of experimental information for the O–ZrO_2 part of the diagram and the equilibrium L/L + ZrO_{2-x} at high temperature.

The enthalpy of formation of the hcp_A3 solid solution at 298.15 K is presented in Fig. 6.

3.3. UO_2–ZrO_2 (uranium oxide–zirconium oxide)

3.3.1. Short presentation of the different phases

Relave et al. [57] optimized the UO_2–ZrO_2 phase diagram and compared it to experimental values from different authors. Yashima et al. [58] presented recently a thermodynamic assessment of the zirconia–urania system by using the CALPHAD (CALculation of PHAse Diagrams) method. We propose here a re-evaluation of the system, based on our selected data for pure oxides, which differs only on details from the previous ones. The

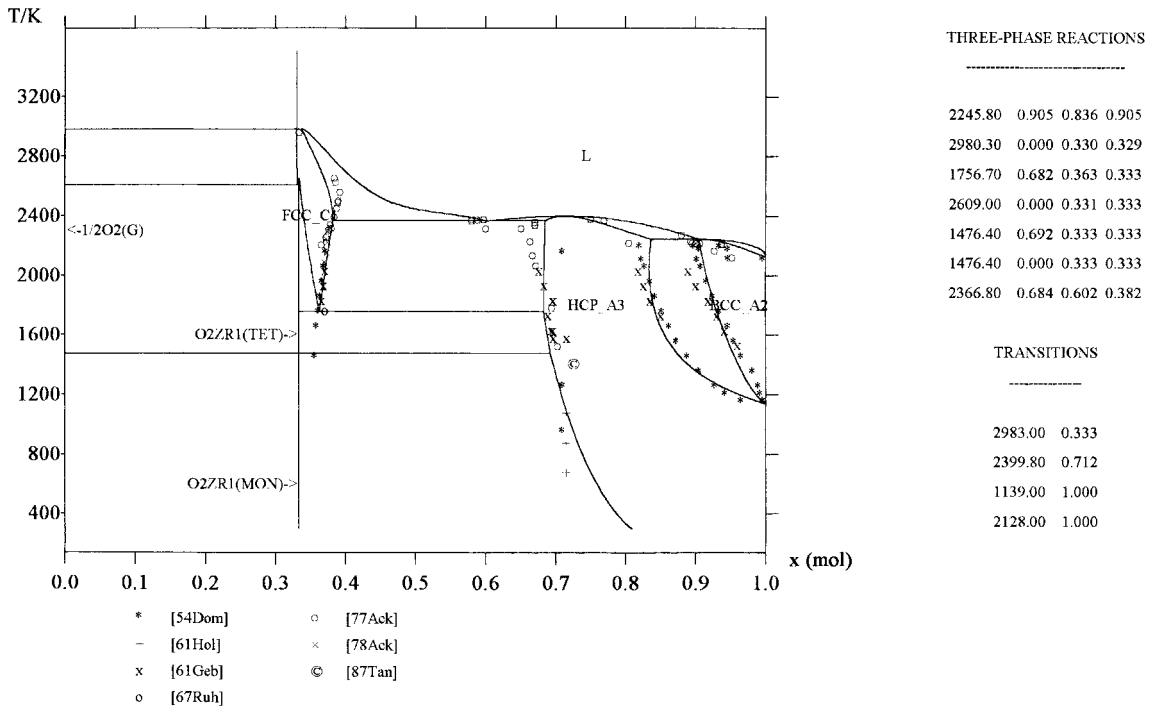

Fig. 5. O–Zr calculated equilibrium phase diagram compared to the experimental information.

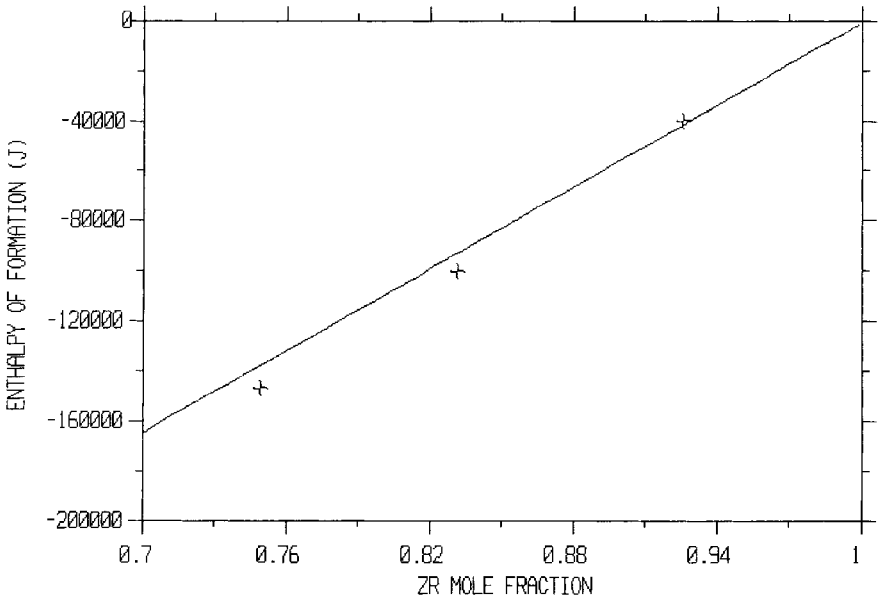

Fig. 6. Calculated enthalpy of formation of the hcp_A3 solid solution compared to the experimental data of Kornilov et al. [53].

condensed solutions and stoichiometric substances, with the symbols currently used in this work, are the following: liquid phase, L; (U, Zr)O_2 solid solution, fcc_C1, cubic; (U, Zr)O_2 solid solution, tet, tetragonal; ZrO_2(mon), monoclinic.

3.3.2. Experimental information

3.3.2.1. Phase diagram. Lambertson and Muller [59] studied the system at high temperatures. Their phase diagram indicates that up to 20 mol% UO_2 is taken into solid solution in ZrO_2 and about 40 mol% ZrO_2 in UO_2 at about 1673 K. The details of the closure of the two-phase area (cubic + tetragonal) are impossible from the phase rule point of view and are also inconsistent with the fact that the high temperature modification of zirconia is cubic and not tetragonal. The minimum of the diphasic equilibrium L ↔ fcc_C1 was located at 2823 K and 52.5 mol% ZrO_2.

Voronov et al. [60] determined by X-ray analysis that the decomposition of the initial solid solution begins at 1943 K. The fcc_C1 / fcc_C1 + tetragonal boundary was determined from lattice parameters studies.

Wolten [61] reached the following conclusions: at 2573 K, a homogeneous phase extends from 0 to 100% ZrO_2, and the cristal structure of this phase changes in a continuous manner from cubic for pure UO_2 to tetragonal for ZrO_2 rich mixtures. At temperatures above 2473 K, the structure remained cubic for samples of increasing ZrO_2 content until 53–54 mol% ZrO_2 was reached, at which point the tetragonal structure was first recognized. The temperature at which pure zirconia transforms from a monoclinic to a tetragonal structure is lowered drastically by additions of urania, to the extent of approximately 100 K per mol% UO_2 added.

Evans [62] proposed a phase diagram on the basis of earlier work and the results of new studies in which the mixed oxides were melted in a solar furnace to avoid contamination. X-ray diffraction measurements were made on specimens melted in helium and on the same specimens after heating to 1623 K in helium. The system shows a narrow two-phase region about the eutectic at high temperatures which increases in extent at lower temperatures. The high-temperature form of zirconia cannot be stabilized by the addition of UO_2. A common feature of all these experimental studies is the fact that the tetragonal–cubic transition of pure zirconia is not well determined.

Cohen and Schaner [63] constructed from metallographic and X-ray studies a new phase diagram, due to the considerable differences apparent among the various investigations of this system. The results indicate a continuous face-centered cubic solution from pure UO_2 to pure ZrO_2 in the temperature range 2573–2823 K, thus confirming the existence of a third cubic polymorphic form of pure ZrO_2 in addition to the tetragonal and monoclinic phases stable at successively lower temperatures. At high temperature two-phase region, previously unreported, has been found to exist above 1933 K in the ZrO_2-rich portion of the phase diagram. The confusion concerning single phase compositions quenched from high temperature and resulting in cubic or tetragonal structures without an intervening two-phase region has been clarified by the discovery of a diffusionless transformation which occurs on cooling compositions of 55

mol% UO_2 or less, and its approximate location was established. The numerical data come from Table 16.

The reported liquidus points come from unpublished data by Wisnyi and Pijanowski [64].

Romberger et al. [65] studied phase equilibria from 873 to 1403 K by agitation of mixtures of the separate oxides or solid solutions of the oxides in the presence of a molten salt solution. After quenching, the oxide phases were freed of fluorides by water washing, separated by dissolution of the UO_2 phase in nitric acid, and then analyzed. From the results it was concluded that at a eutectoid temperature of 1383 ± 5 K, the three equilibrium solid solutions were tetragonal ZrO_2 (2.8 mol% UO_2), monoclinic ZrO_2 (0.2 mol% UO_2) and cubic UO_2 (0.38 mol% ZrO_2), leading to a revised phase equilibrium diagram.

Paschoal et al. [66] have investigated the phase behaviour of the pseudoquaternary $BaO–UO_2–ZrO_2–MoO_2$ system and of pseudo-ternary subsystems at 1973 K under an oxygen partial pressure less then 10^{-7} bar. In the pseudo-binary $UO_2–ZrO_2$ system, cubic (U, Zr)O_2 and tetragonal (Zr, U)O_2 are separated by a broad two-phase region. The maximum solubility of ZrO_2 in UO_2 is 51 mol% ZrO_2, that of UO_2 in ZrO_2 is 21 mol% UO_2 on the basis of X-ray microanalysis data.

3.3.2.2. Thermodynamics. Alexander et al. [67] measured the vapor pressure over a mixture composed of one mole of UO_2 and one mole of ZrO_2. Only UO_2, UO and ZrO were observed over a temperature range 1900–2500 K. The data imply that the reaction is endothermic and leads to development of two phases.

The vaporization processes and thermodynamic properties of the $UO_2–ZrO_2$ system were studied by the isothermal mass spectrometric vaporization method in the temperature range 2200–2650 K by Stolyarova et al. [68]. The activity of UO_2 and ZrO_2 at 2203 and 2498 K has been determined.

3.3.3. Optimization results

3.3.3.1. Numerical data. The assessed values for UO_2(fcc_C1, L) and ZrO_2(fcc_C1, tet, mon, L) have been previously described. All the condensed solutions, liquid, fcc_C1, tetragonal, monoclinic, have been represented by means of a two sublattices model, using the formula $[O_1]_2[U_1, Zr_1]\langle L\rangle$, $[O_1]_2[U_1, Zr_1]\langle$fcc_C1$\rangle$, $[O_1]_2[U_1, Zr_1]\langle$tet$\rangle$, $[O_1]_2[U_1, Zr_1]\langle$mon$\rangle$. The interaction parameters between uranium and zirconium on the second sublattice, $L\_[O_1]_2[U_1, Zr_1]\langle\Phi\rangle$ have been optimized by using the experimental phase diagram information.

3.3.3.2. Graphical outputs. The calculated phase diagram compared to the available experimental information is presented in Fig. 7. The agreement between the calculated phase diagram and the available experimental information is satisfactory, although the tetragonal phase boundary could be improved. Fig. 8 shows the calculated partial potentials of UO_2 and ZrO_2 compared to the experimental ones of Stolyarova et al. [68].

3.4. U–Zr (uranium–zirconium)

3.4.1. Short presentation of the different phases

Sheldon and Peterson [69] and Okamoto [70] presented an assessed phase diagram based on the compilation of experimental available information. The condensed solutions and stoichiometric substances, with the symbols currently used in this work, are the following: liquid phase, L; (γU, β-Zr) solid solution, bcc_A2, body centered cubic ; (β-U) terminal uranium rich solid solution, tet, tetragonal; (α-U) terminal uranium rich solid solution, ort_A20, orthorhombic; (α-Zr) terminal zirconium rich solid solution, hcp_A3, hexagonal compact; δ intermetallic phase, U_3Zr_7(S).

Table 16
Equilibrium fcc_C1 + tetragonal from Cohen and Schaner [63]

	mol% (ZrO_2)					
	fcc_C1			Tetragonal		
T (K)	Metallography		X-ray	Metallography		X-ray
2148	67.5*	68.5	70	81.4*	79.5	79.6
2073	64.8*	69	67.5	80.9*	80.9	80.0
2013	59.5*	59.1	59.2	80.8*	77.6	80.8
1963	51.2*	56.0	57.5	81.2*	80.1	76.7
1933	39.0*	49.5	47.5	81.5*	80.6	81.0
1918	36.0*	45.0	42.5	81.5	81.3*	78.5
1873		27.5*	28.7		83.2	82.6*
1673		14.0*	15.0		83.0*	
1473		13.0*	14.5	84.0	81.0*	

*Results with greater reliance.

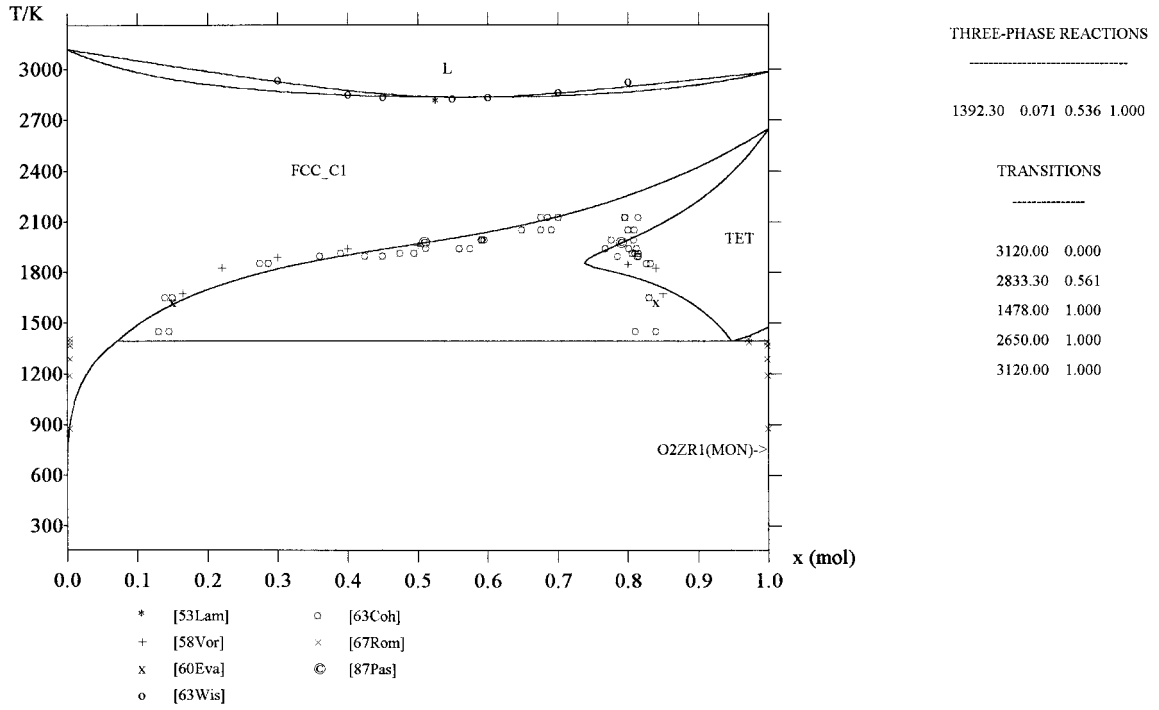

Fig. 7. UO_2–ZrO_2 calculated equilibrium phase diagram compared to the experimental information.

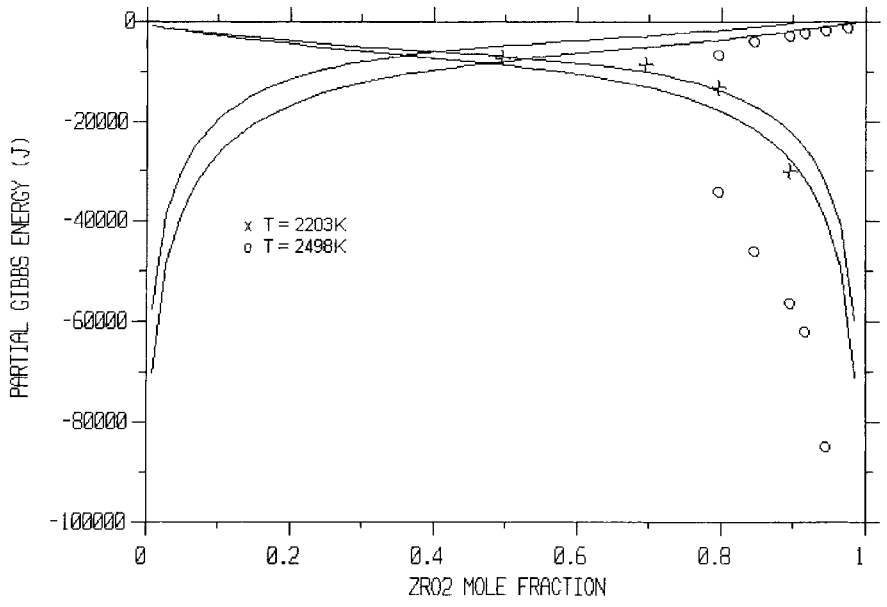

Fig. 8. Calculated partial Gibbs energy of UO_2 and ZrO_2 compared to the experimental ones of Stolyarova et al. [68].

3.4.2. Experimental information

3.4.2.1. Phase diagram. Summers-Smith [71] has examined the uranium–zirconium system by metallographic, dilatometric and X-ray methods, using alloys prepared by arc-melting. A continuous series of body centered cubic solid solutions is formed between γ-uranium and β-zirconium. At 14.5 at.% Zr, the γ phase exists up to 966 ± 3 K, where it undergoes a monotectoid reaction; at 69.5 at.% Zr it exists up to 879 ± 3 K, where it transforms by a eutectoid reaction. A miscibility gap is

formed at 966 K from 14.5 to about 57 at.% zirconium; this reaches a maximum of 1013 ± 3 K and 34 at.% Zr. The maximum solubility of zirconium in β-uranium is 2.5 at.% at 966 K; the β solution transforms by a eutectoid reaction at 935 ± 2 K, with 1.5 at.% Zr. The maximum solubility of zirconium in α uranium at the eutectoid is placed tentatively at about 1 at.%; the eutectoid transformation extends to approximately 61 at.% Zr. The solubility of uranium in α-zirconium is estimated to be 0.75 at.% at 897 K. Liquidus and solidus have been determined by thermal analysis. The melting points of uranium–zirconium alloys are reported in Table 17 from the given numerical data.

Philibert and Adda [72] partially studied the phase diagram by chemical diffusion and give some limits of the bcc_A2 solid solution with other solid phases.

Duffey and Bruch [73] determined the δ phase field on the basis of metallographic and cooling-rate studies of 15 U–Zr alloys. The two invariant reactions bcc_A2 + ort_A20 ↔ δ and bcc_A2 ↔ δ + hcp_A3 are located respectively at 890 and 879 K. The transformation temperatures δ/δ + bcc_A2 and δ + bcc_A2/ bcc_A2 are reported in Table 18.

Zegler [74] determined the limits of the monophasic / diphasic bcc_A2 region as reported by Sheldon and Peterson [69].

Leibowitz et al. [75] reported solidus and liquidus temperatures of a U–19.3 at.% Zr alloy, respectively 1489 ± 7 K and 1631 ± 10 K.

Ohmichi [76] determined the liquidus of three specific compositions, reported by Ogawa and Iwai [77].

Table 17
Melting points of uranium–zirconium alloys from Summers-Smith [71]

x (Zr)	T^S	x (Zr)	T^L
0.10	1433–1473	0.40	1783
0.20	1523–1573	0.50	1833
0.50	1673–1723	0.60	1913
		0.70	1998
		0.80	2083

Table 18
Phase boundaries of the δ/bcc_A2 region from Duffey and Bruch [73]

wt% (Zr)	x (Zr)	T (K) (upper)	T (K) (lower)
40	0.635	889.15	886.05
44	0.672	890.65	883.15
46	0.690	889.15	880.45
48	0.707	885.95	878.95
50	0.723	884.45	878.25
52	0.738	884.25	878.15
54	0.754	882.55	877.55
58	0.781	880.45	878.25
60	0.796	880.65	878.15

Maeda et al. [78] determined two other liquidus points, reported by Okamoto [70].

Akabori et al. [79] examined homogeneity range and crystal structure of the intermediate δ phase in the U–Zr alloy by electron probe microanalysis, X-ray diffraction and differential thermal analysis, using the alloys prepared by arc-melting. The homogeneity range of the δ phase was found to be 64.2–78.2 at.% Zr at 873 and 66.5–80.2 at.% Zr at 823 K. The metallographic results of Howlett and Knapton [80] have been reported by the previous authors as 63–79.5 at.% Zr at 873 K and 66–79 at.% Zr at 773 K.

3.4.2.2. Thermodynamics. Kanno et al. [81] studied vaporization of a series of U–Zr alloys by using a tantalum Knudsen cell coupled with a mass spectrometer in the temperature range 1700–2060 K. Thermodynamic activities, partial molar Gibbs free energies and integral molar Gibbs free energies of mixing were calculated from the partial vapor pressures of uranium over these alloys. Composition of the liquidus and solidus were estimated at three temperatures. The activities of uranium exhibit negative deviations from ideality, especially in the uranium-rich composition region. These values were reported in Table 19.

Leibowitz et al. [82] propose the activity coefficients of uranium to be close to unity even in the liquid phase by the thermodynamic analysis of the uranium–zirconium system.

Maeda et al. [78] determined the uranium activities of two U–Zr alloys of uranium-rich composition (24.4 and 39.3 at.% Zr) by means of the Knudsen cell-mass spectrometer method.

Nagarajan et al. [83] determined the enthalpy of formation of the intermetallic compound UZr_2 at 298 K by high temperature solution calorimetry in which liquid aluminium was used as the solvent: $\Delta H_{298.15}(UZr_2) = -4.0 \pm 10.1$ kJ/mol. The enthalpy of formation of the intermetallic compound UZr_2 at 298 K was also reported by Ogawa [77]: $\Delta H_{298.15}(UZr_2) = -1.3 \pm 3.4$ kJ/mol.

3.4.3. Optimization results

3.4.3.1. Numerical data. All the condensed solutions, liquid, bcc_A2, hcp_A3, tetragonal and monoclinic,

Table 19
Thermodynamic activities and partial molar Gibbs energies at 1773 K from Kanno et al. [81]

x (Zr)	a_U	ΔG_U (J/mol)	a_{Zr}	ΔG_{Zr} (J/mol)
0.902	0.029	−52 191	0.861	−2206
0.715	0.221	−22 254	0.571	−8261
0.522	0.231	−21 601	0.557	−8626
0.346	0.384	−14 109	0.240	−21 038
0.140	0.784	−3587	0.033	−50 287

have been represented by means of a classical substitutional model, using the formula $[U_1, Zr_1]\langle\Phi\rangle$. The Gibbs energy of the pure stable reference components has been previously described. The one of the metastable reference components Zr_1(tet) and Zr_1(ort_A20) has been estimated. In a first step, we have not modelled the large domain of non-stoichiometry of the δ phase, and considered it as a stoichiometric compound, U_3Zr_7(S). This will be made in the final assessment, but in any case, it is not fundamental in the temperature range of an hypothetical severe accident. The interaction parameters between U_1 and Zr_1 have been optimized by using the experimental phase diagram information. The liquidus and solidus data estimated by Kanno et al. [81] are not in good agreement with the rest of the available experimental information. Moreover, the high negative deviation from ideality of the activity of uranium at 1773 K according to these authors is compatible with difficulty with the existence of a miscibility gap in the solid phase at lower temperature. The enthalpy of formation of the δ phase at room temperature has been fixed to the experimental one of Nagarajan et al. [83].

3.4.3.2. Graphical outputs. The agreement between the calculated phase diagram and the available experimental information, presented in Fig. 9, is quite satisfactory.

The calculated partial Gibbs energy of uranium in the liquid phase is compared to the experimental one of Kanno et al. [81] and Maeda et al. [78] in Fig. 10. The calculated values show a positive deviation from ideality, contrarily to the experimental ones, which cannot be easily conciliated with the experimental phase diagram without including unlikely excess Gibbs energy parameters.

4. O–U–Zr ternary system

4.1. Short presentation of the different phases

The different possible condensed phases resulting from the analysis of the binary or pseudo-binary subsystems are the following: the ternary liquid phase, L, may present a miscibility gap on the uranium–uranium dioxide side at high temperature; the ternary intermediate oxide cubic face-centered solid solution, fcc_C1, fluorite type, $(U, Zr)O_{2\pm x}$; the ternary intermediate oxide tetragonal solid solution, tet(oxide), $(U, Zr)O_2$; the ternary terminal metallic body centered cubic solid solution, bcc_A2, which may dissolves 10 at.% O at maximum on the zirconium rich side (uranium and zirconium form a continuous solid solution at high temperature and a miscibility gap at lower temperature); the ternary terminal metallic hexagonal compact solid solution, hcp_A3, which may dissolves 35 at.% O at maximum on the zirconium rich side and has a very limited uranium content (about 2 or 3 at.%); the binary terminal uranium rich tetragonal solid solution, tet(metal), with a very limited zirconium content; the

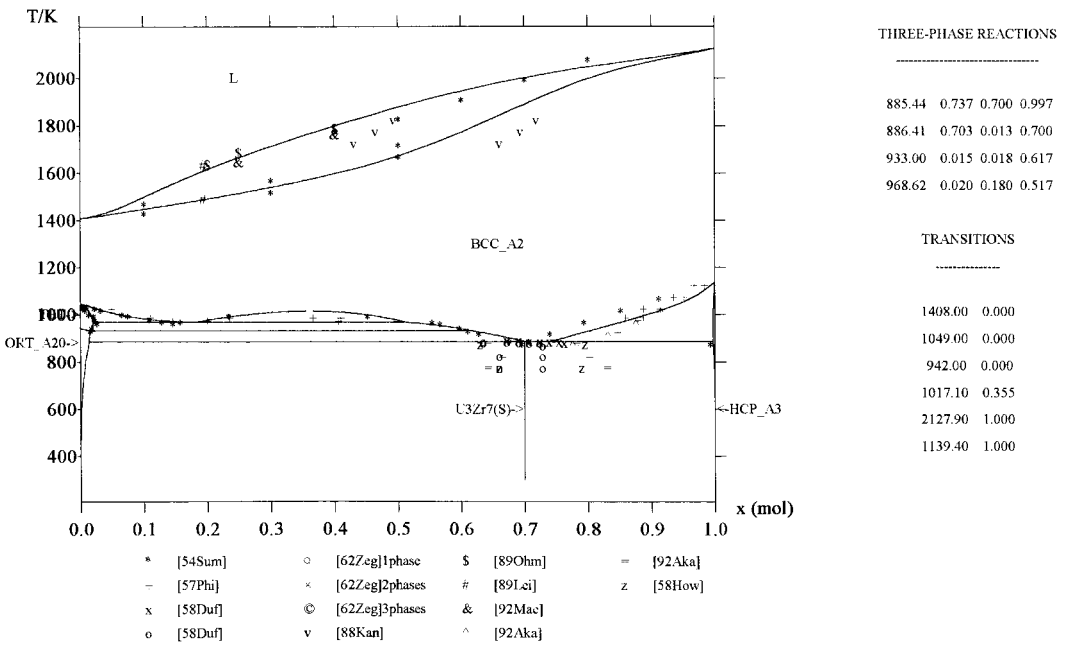

Fig. 9. Calculated U–Zr equilibrium phase diagram compared to the available experimental information.

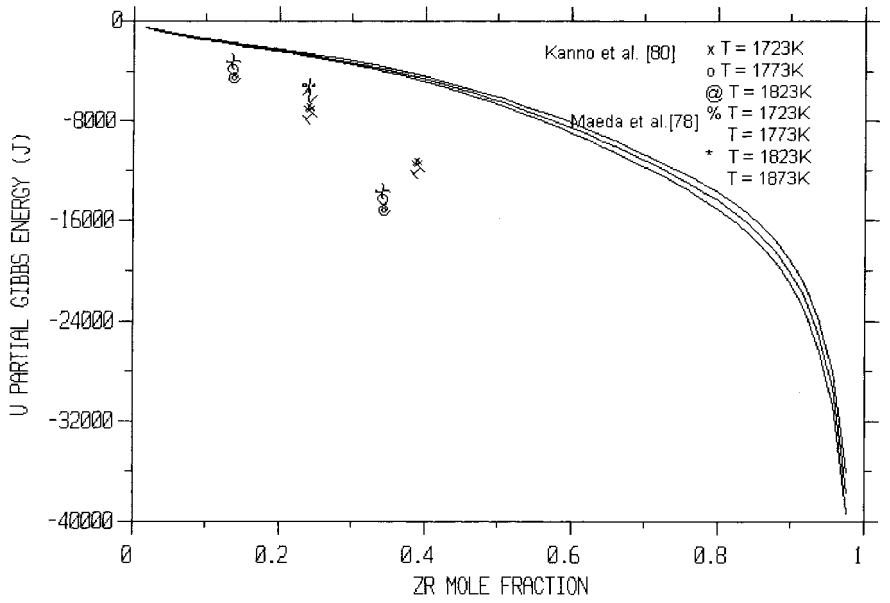

Fig. 10. Calculated U partial Gibbs energy (J) compared to the experimental one.

binary terminal uranium rich orthogonal solid solution, ort_A20, with a negligible zirconium content; the pure oxides U_3O_8(S), U_4O_9(S), UO_3(S) and ZrO_2(monoclinic), all considered as stoichiometric.

4.2. Experimental information

Although the ternary O–U–Zr system has been often studied, the resulting information appears to be scarce and some points of controversy remain, especially at high temperatures (above 2000 K).

Politis [85] made a first compilation of the available experimental information. He presented all the binary U–Zr, Zr–ZrO_2, U–O, U–UO_2 and pseudo-binary UO_2–ZrO_2 subsystems, that we have previously discussed, and some partial results in the ternary system.

The isothermal section at 1368 K of Saller et al. [84] showed the following phase regions: UO_2 + (γU–βZr) + α-Zr, UO_2 + α-Zr, (γU–βZr) + α-Zr, UO_2 + ZrO_2 + α-Zr, ZrO_2 + α-Zr, UO_2 + ZrO_2, UO_2, α-Zr, (γU–βZr).

Three other isothermal sections are given by Politis [85]: UO_2 + ZrO_2 + α-Zr, UO_2 + (γU–βZr) + α-Zr, (γU–βZr) + α-Zr, UO_2 + (γU–βZr), U_3O_8 are reported at 1273 K; UO_2 + ZrO_2 + α-Zr, UO_2 + α-Zr + L, UO_2 + L, α-Zr + L, α-Zr + (γU–βZr) + L, α-Zr + (γU–βZr), α-Zr, (γU–βZr), L, UO_2, ZrO_2 at 1773 K; (U, Zr)O_{2-x} + L, L, (U, Zr)$O_{2\pm x}$, ZrO_2(tet), ZrO_{2-x} (cub) at 2273 K. Experimental points are given for the last section. In the two-phase field (U, Zr)O_{2-x} + L: [x(O), x(U), x(Zr)] = 0.6, 0.1, 0.3; 0.6, 0.2, 0.2; 0.6, 0.3, 0.1; 0.55, 0.1, 0.35; 0.55, 0.2, 0.25; 0.55, 0.3, 0.15; 0.45, 0.05, 0.5; 0.45, 0.1, 0.45; 0.45, 0.15, 0.4; 0.35, 0.25, 0.4; 0.35, 0.35, 0.3; 0.35, 0.45, 0.2. And in the monophasic liquid region: 0.4, 0.05, 0.55; 0.35, 0.05, 0.6; 0.35, 0.15, 0.5; 0.3, 0.25, 0.45. These sections were also reported by Hofman and Politis [87].

The pseudo-binary α-Zr(O)–UO_2 section, which shows a miscibility gap in the liquid state, was presented both by Politis [85], and Hofman et al. [86]. In this section, a monotectic reaction L2 ↔ L1 + (U, Zr)O_{2-x} occurs at 2673 K, and a eutectic one L1 ↔ α-Zr(O) + UO_2 at about 2113 K. The experimental points (mol% UO_2: T(K)) were determined to be in the following domains: α-Zr(O) + UO_2 (25: 1873, 2073; 50: 1873, 2073; 95: 1873; 96.5: 1873), L1 (5: 2123, 2173, 2273; 10: 2373, 2573; 15: 2573), L1 + (U, Zr)O_{2-x} (10: 2123, 2173, 2273; 25: 2123, 2173, 2273, 2573; 50, 2173, 2273, 2573; 70, 2573), L1 + L2 (25: 2700; 50: 2700, 2773; 82.5: 2700, 2773; 85: 2700), L2 (85: 2773; 90: 2873; 95: 3023), L2 + (U, Zr)O_{2-x} (90: 2700, 2773; 95: 2873, 2973), (U, Zr)O_{2-x} (95: 2673, 2700, 2773; 96.5: 2173; 98.5: 2173).

The true composition of the α-Zr(O) phase on the left side of the diagram is not clearly mentioned. It could be supposed to be the one of pure zirconium (as indicated by the melting point near to 2128 K), but more probably the one of oxygen stabilized alpha phase zirconium, as suggested by Hagrman et al. [88] (melting point corrected at about 2473 K), which is temperature-dependent, but around $Zr_{0.7}O_{0.3}$ (or $ZrO_{0.43}$). The 'tentative' Zr–UO_2 diagram proposed by Juenke and White [89] was not used in the optimization procedure.

There is a noticeable inconsistency between the diagram of this subsystem [85,86] and the isothermal section at 2273 K [85,87]. The solubility limit is esti-

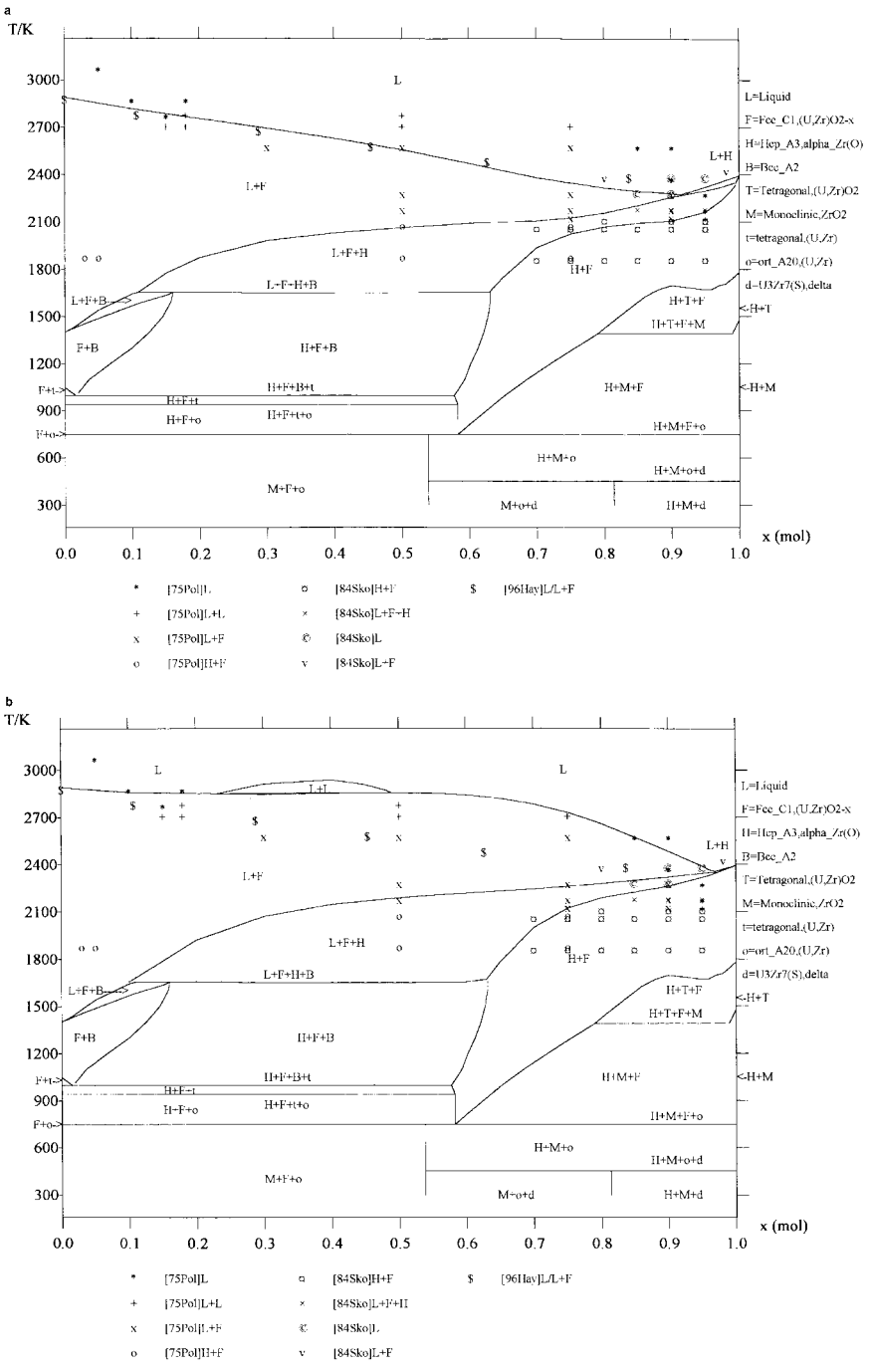

Fig. 11. (a) Calculated pseudo-binary $UO_{1.7}$–$ZrO_{0.43}$ sections compared to the available experimental information [85,90,96], with the set of parameters (a). (b) Calculated pseudo-binary $UO_{1.7}$–$ZrO_{0.43}$ sections compared to the available experimental information [85,90,96], with the set of parameters (b).

mated to be 14 mol% UO_2 from the isothermal section at 2273 K, whereas equal to 8 mol% UO_2 in the pseudo-binary section. The melting point of O-saturated Zr is quoted at about as 2148 K, which is lower both than the one given by Domagala and McPherson [43] (2248 K) and Ackermann et al. [44] (2403 K).

Skokan [90] proposed a revised temperature-concentration diagram of the pseudo-binary system

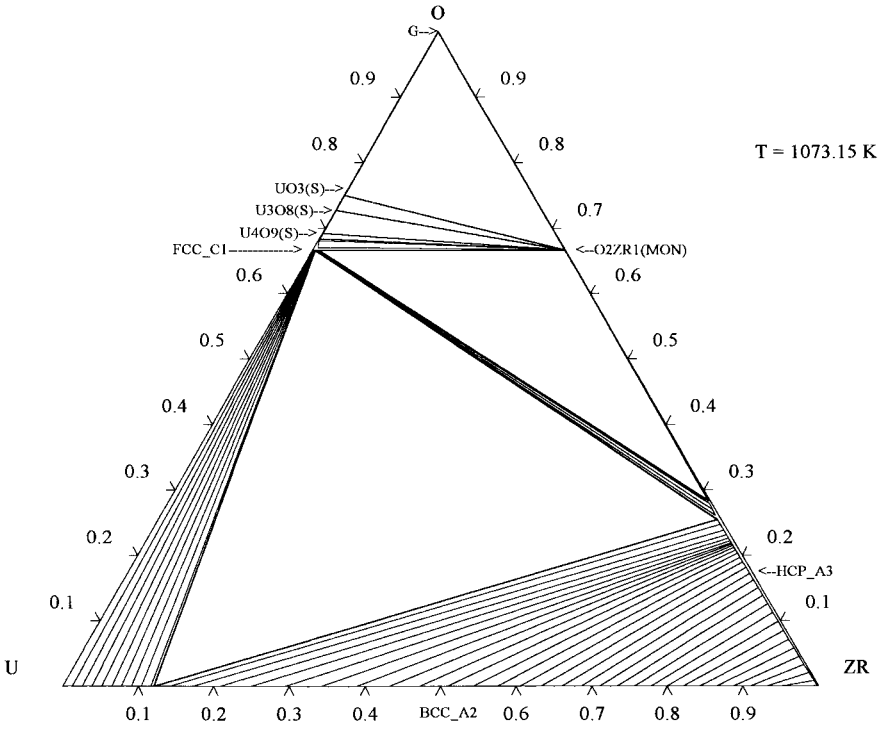

Fig. 12. Calculated O–U–Zr phase diagram at 1073 K.

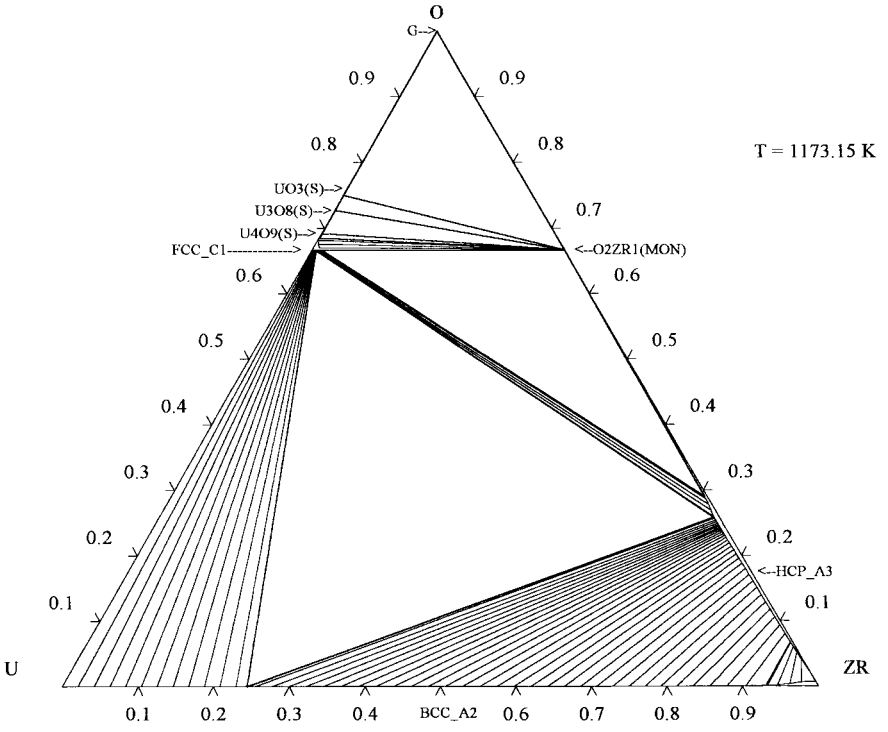

Fig. 13. Calculated O–U–Zr phase diagram at 1173 K.

α-Zr(O)–UO_2. For the revised phase diagram, the oxygen concentration in α-Zr(O) was fixed at 30 at.% instead of 34 at.% by Politis [86]. A new eutectic temperature of 2173 K, 60 K higher than the previous result has been measured. In this work, the liquidus line of the two-phase field (U, Zr)O_{2-x} + L on the Zr-rich side is shifted to higher UO_2 contents. The results show that the maximum amount of UO_2 which can be dissolved at 2273 K is about 16 mol%. This value agrees with the phase field distribution in the isothermal section O–U–Zr at 2273 K significantly better than the earlier value of 8 mol%. The limit of solubility of UO_2 in $ZrO_{0.43}$ has been determined in the range 1873–2373 K. The experimental points (mol% UO_2: T(K)) were determined to be in the following domains: α-Zr(O) + (U, Zr)O_{2-x} (5, 10, 15, 20, 25: 1873, 2073; 5, 10, 20: 2123), α-Zr(O) + (U, Zr)O_{2-x} + L_(5, 10, 15: 2173), α-Zr(O) + L (5: 2223), L (10, 15: 2273; 5, 10: 2323), L + (U, Zr)O_{2-x} (20: 2323, 2373). The melting point of O-saturated Zr is about 2273 K, which agrees better with the one of Domagala and McPherson [43] than the one of Ackermann et al. [44]. Two other isothermal sections were reported with the following domains: (U, Zr)O_{2-x} + α-Zr(O), UO_2 + α-Zr(O) + L, UO_2 + L, L + α + β, α + β, UO_2, ZrO_2 (te, k), α-Zr(O), L,β, O at 1873 K; (U, Zr)O_{2-x} + α-Zr(O), UO_2 + L, UO_2, ZrO_2 (te, k), α-Zr(O), L, β, O at 2073 K. No experimental points are given for these sections.

Yamanaka et al. [91] studied the reaction between UO_2 and Zr from both equilibrium and kinetic points of view. In the equilibrium study, the reaction between UO_2 and Zr with several Zr/UO_2 mole ratios has been made at 1273 K and the products have been identified using X-ray diffraction method. The interfacial reaction zones after the heat-treatment of the reaction couples of UO_2 pellet and Zr sheet have been studied using a SEM. A tentative isothermal section of the O–U–Zr system at 1273 K is proposed with the following phase regions: α-Zr(O) + (U–Zr); α-Zr(O) + (U–Zr) + UO_2; α-Zr(O) + UO_2; α-Zr(O) + UO_2 + ZrO_2; UO_2 + ZrO_2; UO_2 + (U–Zr).

The purpose of the further study of Yamanaka et al. [92] was to clarify whether or not the formation of a liquid phase can be caused by the reaction of Zr with UO_2 at high temperatures and to examine the phase regions and boundaries. The isothermal section at 1673 K was proposed and the liquid phase was confirmed to exist in this section. The topology of this section is consistent with Politis' results [76] at 1773 K: the following domains are present: UO_2 + T-ZrO_2; UO_2 +

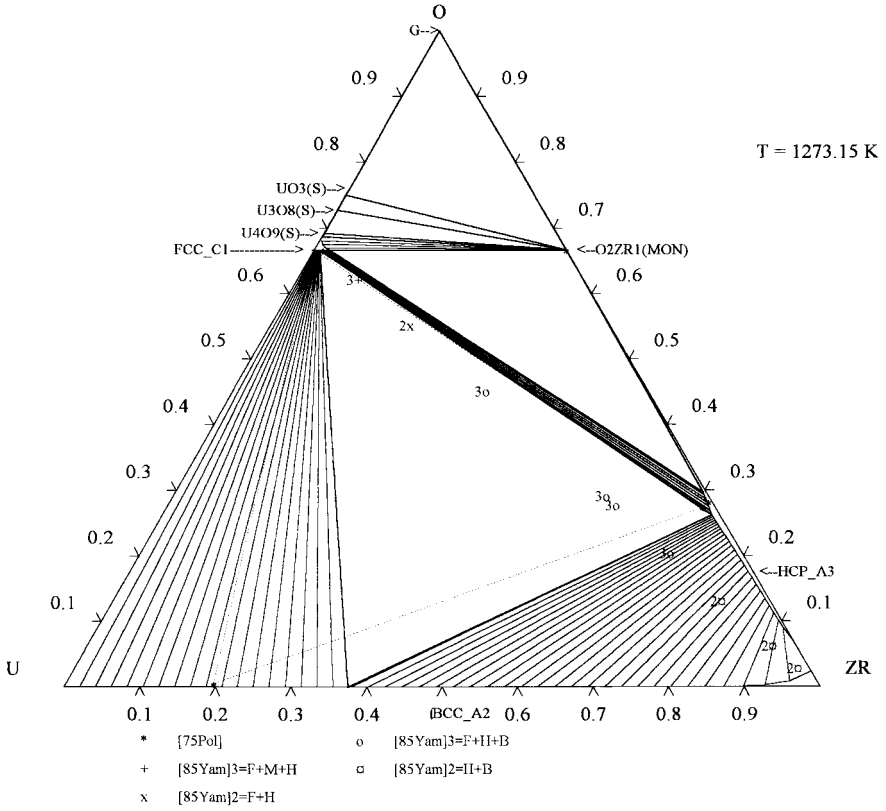

Fig. 14. Calculated and experimental O–U–Zr phase diagram at 1273 K.

T-ZrO_2 + α-Zr(O); UO_2 + α-Zr(O); UO_2 + α-Zr(O) + L; UO_2 + L; α-Zr(O) + L; α-Zr(O) + L + (-γU–βZr); α-Zr(O) + (γU–βZr). A small solubility of uranium in the α-Zr(O) phase is reported.

Miyake et al. [93] made a considerable amount of experimental work with the same method than the previous authors to construct the isothermal sections of the U–Zr–O system at 1273 K and 1673 K. Phase relationships were obtained from X-ray diffraction analysis and metallographic results for the products of the reactions Zr / UO_2 and Zr / ZrO_2 / UO_2. The locations of the phase boundaries were determined from the kind and number of phases in the reaction products and changes in the lattice parameters of α-Zr. The oxygen concentration of α-Zr evaluated from the lattice parameters was found to be strongly dependent on the phase region. The phase regions are the following at 1273 K: UO_2 + M-ZrO_2; UO_2 + M-ZrO_2 + α-Zr(O); UO_2 + α-Zr(O); UO_2 + α-Zr(O) + (γU–βZr); UO_2 + (γU–βZr); α-Zr(O) + (γU–βZr).

Hofmann et al. [94] presented in a new compilation the Zr–ZrO_2 system, isothermal sections of the ternary O–U–Zr system at 1773 K, 1873 K, 2073 K and 2273 K, and the pseudo-binary section α-Zr(O)–UO_2. The main difference with the previous compilation of Politis [86] is the reactualisation of this last section by the work of Skokan [90].

Hayward and George [95,96] have determined the solubilities of nonirradiated UO_2 in molten Zircaloy-4 and in a molten Zircaloy-4 containing 25 at.% O from crucible-based experiments at 100 K intervals over the temperature range 2273–2773 K. Results are presented by using the ratio $S_U = U / (U + Zr)$ wt%, because of uncertainty in melt O concentrations. In all cases, U-saturated melts are formed within a few minutes at temperature. Fuel solubilities increase significantly with rising temperature and, at any one temperature, are highest with initially unoxidized Zircaloy-4 and when the initial UO_2 / Zircaloy-4 mass ratios are low. The saturated melt compositions for the two pseudo-binary α-Zr(O)–UO_{2-x} phase diagrams (the first corresponding to pure Zr and the second to $ZrO_{0.54}$) were calculated by supposing that one mole of dissolved uranium brings $2 - x$ mole of oxygen to the melt. The UO_{2-x}–$ZrO_{0.54}$

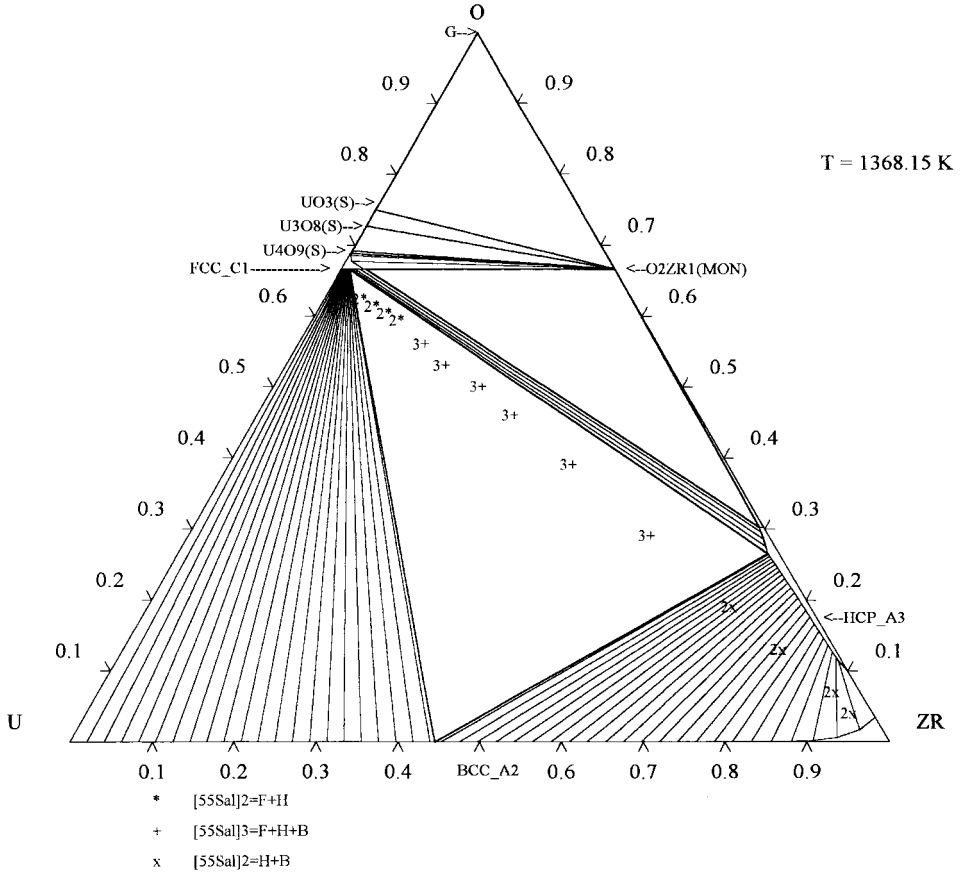

Fig. 15. Calculated and experimental O–U–Zr phase diagram at 1368 K.

vertical section has been graphically reported in the original paper [90], allowing more realistic prediction of the products formed by fuel / molten cladding interaction. The composition of the liquid phase in the ternary system can be deduced from the pseudo-binary values. The composition of the ceramic phase (U, Zr)O_{2-x} was deduced from the original table [95]: T(K), $x(O)^{fcc\_C1}$, $x(U)^{fcc\_C1}$, $x(Zr)^{fcc\_C1} = 2373$, 0.640, 0.241, 0.119; 2473, 0.613, 0.267, 0.120; 2573, 0.631, 0.247, 0.122; 2673, 0.625, 0.273, 0.101; 2773, 0.638, 0.279, 0.083 for $ZrO_{0.54} = 2273$, 0.643, 0.314, 0.043; 2373, 0.645, 0.277, 0.078; 2473, 0.648, 0.299, 0.053; 2573, 0.647, 0.276,

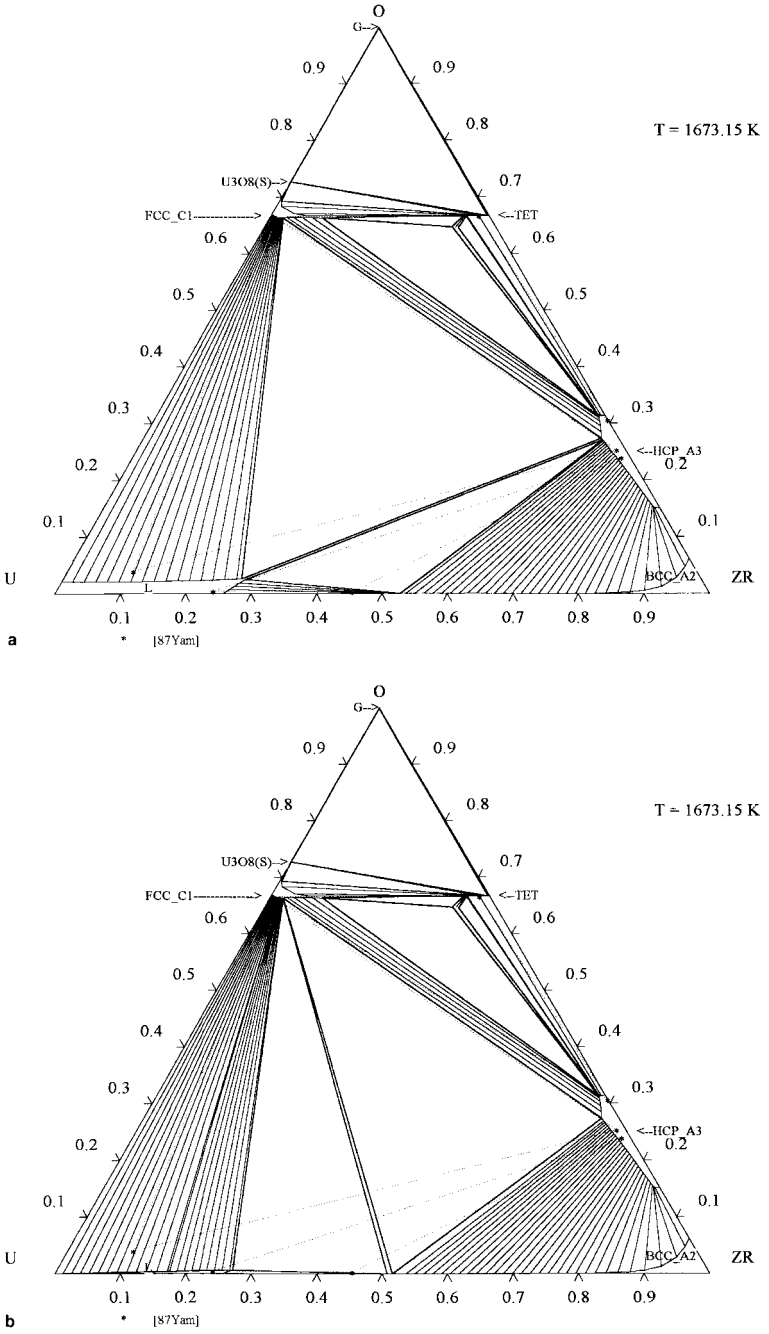

Fig. 16. (a) Calculated (parameters a) and experimental O–U–Zr phase diagram at 1673 K. (b). Calculated (parameters b) and experimental O–U–Zr phase diagram at 1673 K.

0.078; 2673, 0.628, 0.305, 0.067; 2773, 0.628, 0.297, 0.074 for Zr. In contrast to Skokan [80], these authors observed no microstructural evidence or step changes in solubility to indicate the presence of a two-liquid region in the $Zr_y(O)$–UO_{2-x} system. Also Skokan gives the melting point of O-saturated Zr as 2273 K; they observed the melting point of O-saturated Zr_y (indicated by a small endothermic peak on the time/temperature trace recorded during sample heating) to be within the range 2323–2353 K, which is closer than the one of Ackermann et al. [44] than the one of Domagala and McPherson [43].

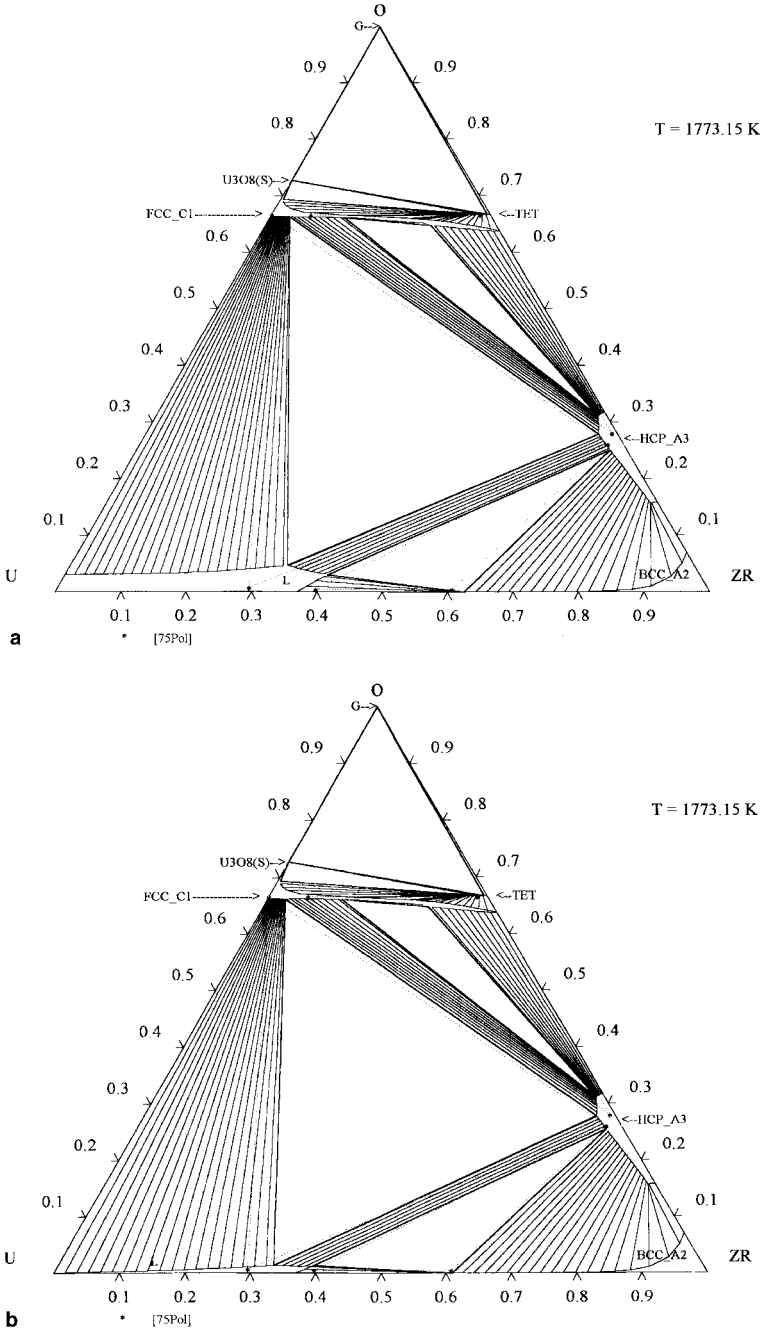

Fig. 17. (a) Calculated (parameters a) and experimental O–U–Zr phase diagram at 1773 K. (b) Calculated (parameters b) and experimental O–U–Zr phase diagram at 1773 K.

Maurisi et al. [97] used the Knudsen effusion mass-spectrometric method to determine the liquidus position for a (U, Zr, O) alloy representative of the corium (U/Zr = 1.35). This study has led to the experimental determination of the oxygen solubility limit in the (U, Zr, O) liquid in the range 2020–2320 K for U/Zr = 1.5. This experimental value (7 at.%) is lower than the 20 at.% estimated one of Politis at 2273 K [85].

All these studies show some points of controversy: first, the low solubilities values of O in U–Zr alloys

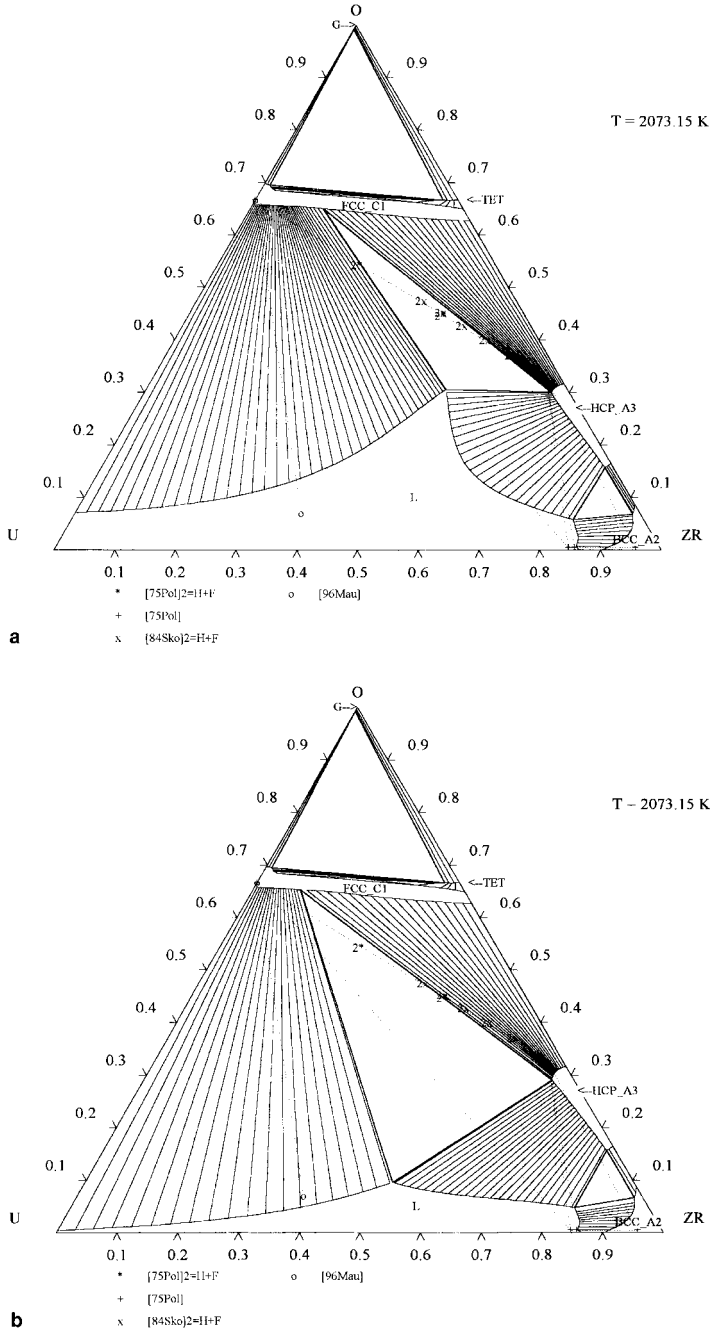

Fig. 18. (a) Calculated (parameters a) and experimental O–U–Zr phase diagram at 2073 K. (b) Calculated (parameters b) and experimental O–U–Zr phase diagram at 2073 K.

determined by Politis [85] and Maurisi et al. [97] (2020–2320 K), seems to be in contradiction with the higher ones of Hofman and Politis [87] (2273 K), Skokan [90] (2273–2473 K) and Hayward and George [96] (2373–2773 K); second the existence of a liquid miscibility gap in the pseudo-binary section UO_{2-x}–α(ZrO), presented by Politis [85] and extrapolated by Skokan [90], is called in question by the recent work of Hayward and George [96].

4.3. Optimization results

The ternary liquid phase has been represented by means of a non-ideal associate model, using the formula

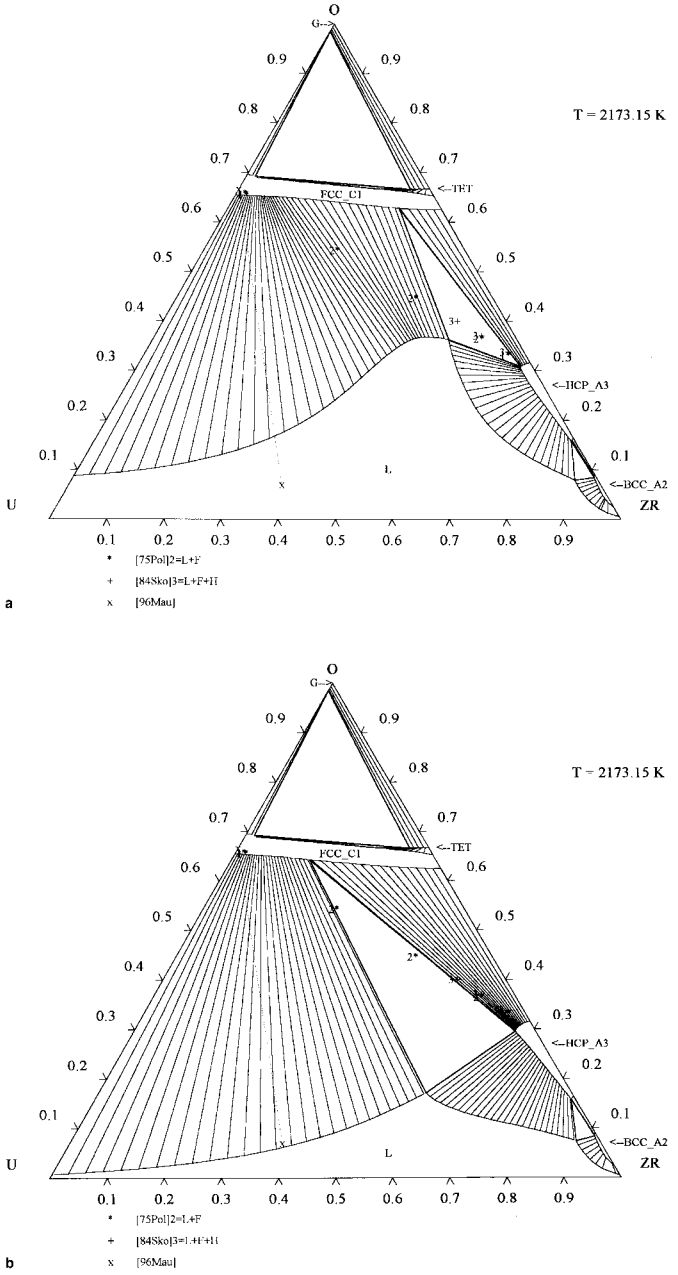

Fig. 19. (a) Calculated (parameters a) and experimental O–U–Zr phase diagram at 2173 K. (b) Calculated (parameters b) and experimental O–U–Zr phase diagram at 2173 K.

$[O_1, O_2U_1, O_2Zr_1, U_1, Zr_1]$ ⟨L⟩. The liquid phase may present a miscibility gap on the uranium–uranium dioxide side at high temperature, which extends in the ternary system. The different binary or ternary metallic and oxide solid solutions have been represented by means of the two-sublattice model, by using the following formula: $[O_1, Va]_2$ $[U_1, Zr_1, Va]_1$ ⟨fcc_C1⟩, $[O]_2$ $[U_1, Zr_1]_1$ ⟨tet⟩, $[O]_2$ $[U_1, Zr_1]_1$ ⟨mon⟩, $[O_1, Va]_2$ $[U_1, Zr_1]_1$ ⟨hcp_A3⟩, $[O_1, Va]_3$ $[U_1, Zr_1]_1$ ⟨bcc_A2⟩. The metallic bcc_A2 solid solution presents a miscibility gap at low temperature on the uranium–zirconium side. Most of the parameters required by the used models come from the critical assessment of the binary or pseudo-binary subsystems. The remaining unknown ternary parameters

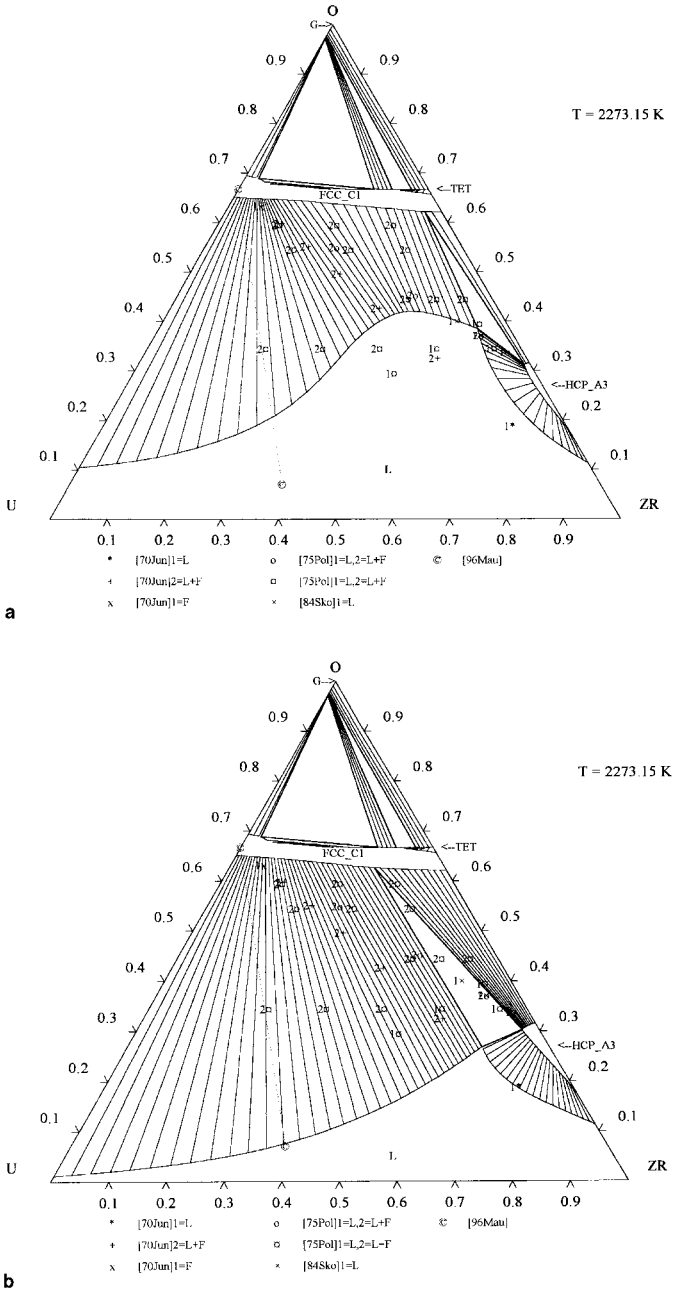

Fig. 20. (a) Calculated (parameters a) and experimental O–U–Zr phase diagram at 2273 K. (b) Calculated (parameters b) and experimental O–U–Zr phase diagram at 2273 K.

are $L[O_2U_1, Zr_1]$ ⟨L⟩, $L[U_1, O_2Zr_1]$ ⟨L⟩, $L[Va_1]_2$ $[U_1, Zr_1]_1$ ⟨fcc_C1⟩, $L[O_1]_2$ $[U_1, Zr_1]_1$ ⟨hcp_A3⟩, $L[O_1]_2$ $[U_1, Zr_1]_1$ ⟨bcc_A2⟩ and are noted with an asterix in Appendices A and B. For the liquid phase, the use of pure or associate species leads to ternary interactions between O_2U_1 and Zr_1 on the one hand and U_1 and O_2Zr_1 on the other hand. For the metal–oxygen solid solutions, the use of the two sublattice model leads to separate a metallic lattice and an oxide lattice. For the oxide fcc_C1 phase, the interaction between uranium and zirconium on the metallic lattice is fictive, as the one on the oxide lattice for the metallic bcc_A2 and hcp_A3 phases. All

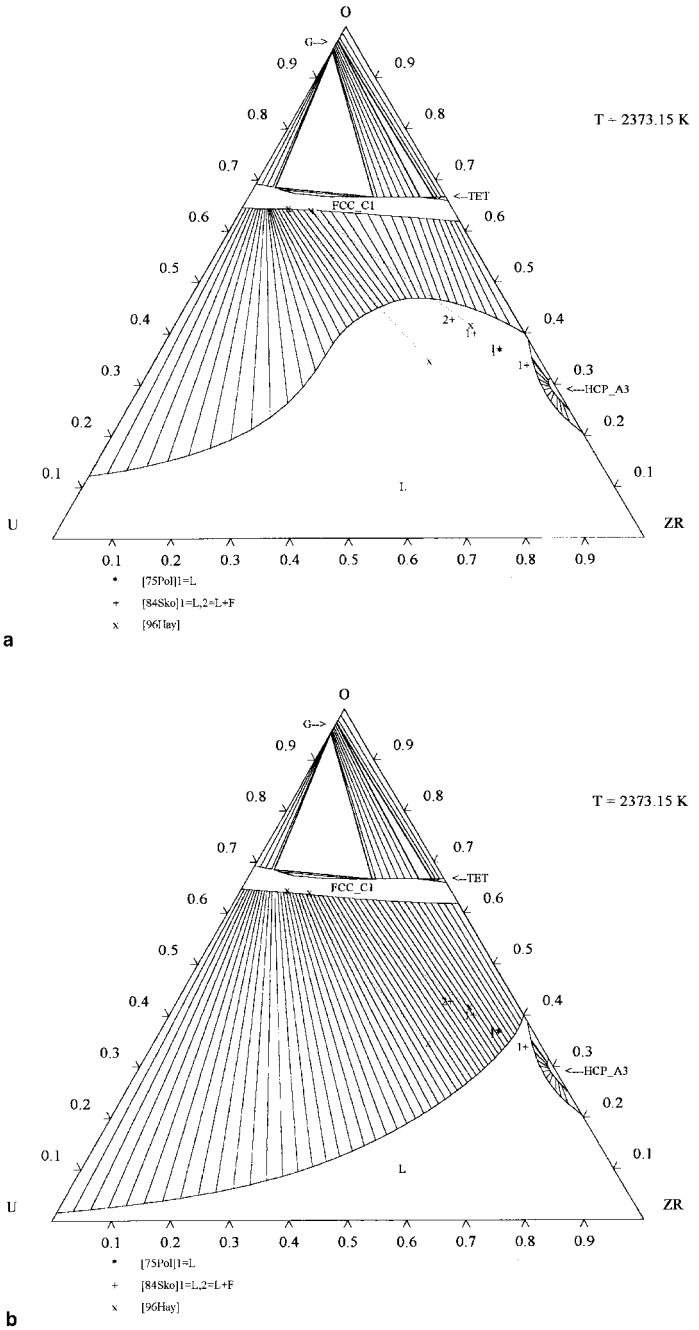

Fig. 21. (a) Calculated (parameters a) and experimental O–U–Zr phase diagram at 2373 K. (b) Calculated (parameters b) and experimental O–U–Zr phase diagram at 2373 K.

these parameters have been estimated either by means of physical considerations, either adjusted on phase diagram boundaries. From a general point of view, the best model should be the one which would require the minimal number of adjustable parameters, by keeping in mind the final aim of using it in more complex systems.

In the thermodynamic modelling, we have observed that both the solubility of oxygen in uranium–zirconium alloys and the extent of the liquid miscibility gap in the ternary system, are tightly linked, first evidently to the extent of the O–U liquid miscibility gap determined by the binary parameter $L[O_2U_1, U_1]\ \langle L\rangle$, and then to the

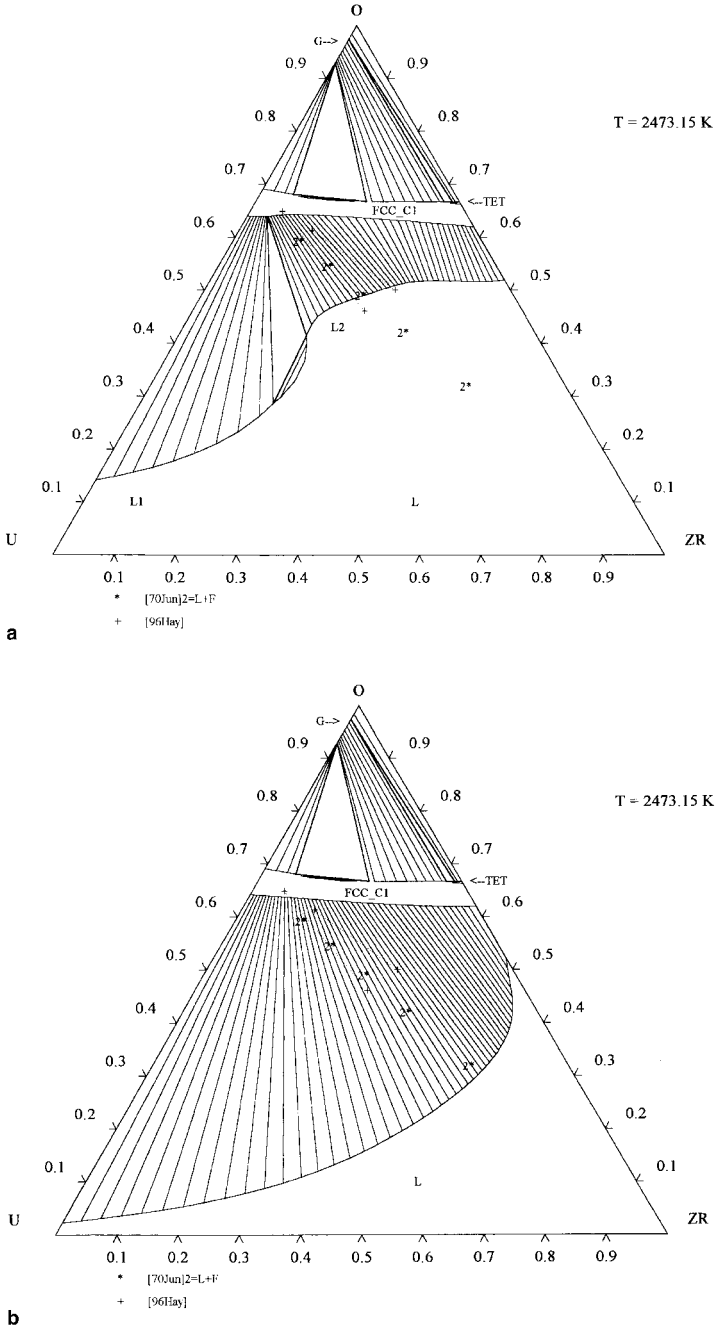

Fig. 22. (a) Calculated (parameters a) and experimental O–U–Zr phase diagram at 2473 K. (b) Calculated (parameters b) and experimental O–U–Zr phase diagram at 2473 K.

adjustable ternary parameters $L[U_1, O_2Zr_1]$ ⟨L⟩ and more especially $L[O_2U_1, Zr_1]$ ⟨L⟩.

As we have already discussed in Section 3.1.3, we have proposed two different versions of the O–U phase diagram: (a) with a solubility of oxygen in liquid uranium in agreement with the Garg and Ackermann's experimental point [22]; (b) with a smaller solubility similar to the one of Martin and Edwards [16]. The miscibility gap is evidently larger in the second case than in the first one. The final choice could result of new available experimental information. Thus, we have used two different set of parameters for the ternary system: (a) $L[O_2U_1, Zr_1]$

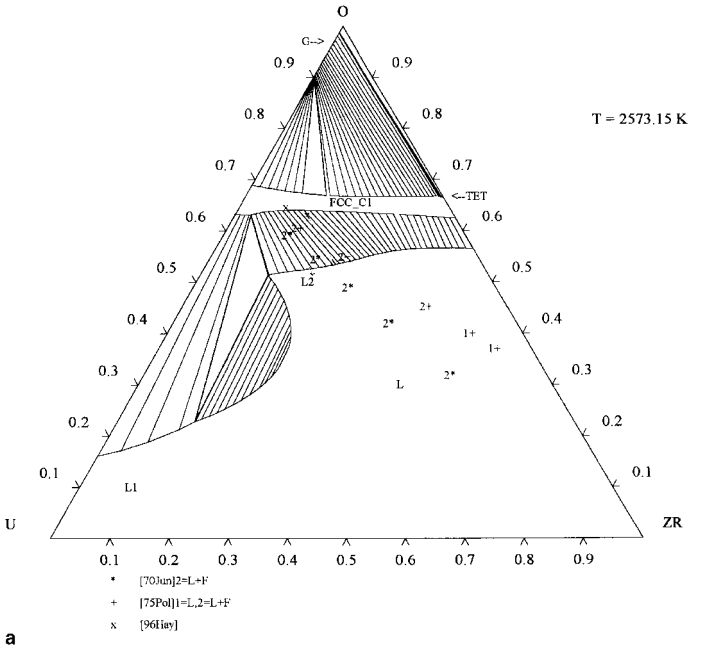

a

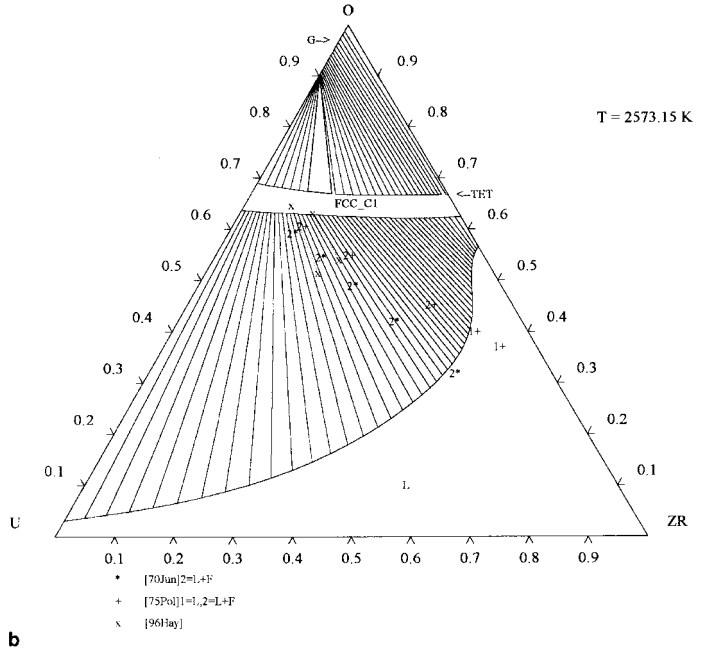

b

Fig. 23. (a) Calculated (parameters a) and experimental O–U–Zr phase diagram at 2573 K. (b) Calculated (parameters b) and experimental O–U–Zr phase diagram at 2573 K.

$\langle L\rangle = 0$ associated to the case (a) for the O–U system; (b) $L[O_2U_1, Zr_1]\ \langle L\rangle = 70\ 000$, associated to the case (b) for the O–U system; the more positive interaction parameter allow to model a miscibility gap in the UO_2–α(Zr–O) vertical section, and a low solubility of oxygen in U–Zr alloys, while the other leads to higher solubilities of oxygen and a smaller extent of the O–U binary miscibility gap into the O–U–Zr ternary system. It has been adjusted by using the experimental solubility of oxygen in the liquid of Maurisi et al. [97] and Politis [85].

Thus, this thermodynamic modelling allows one to calculate the O–U–Zr equilibrium phase diagram in the

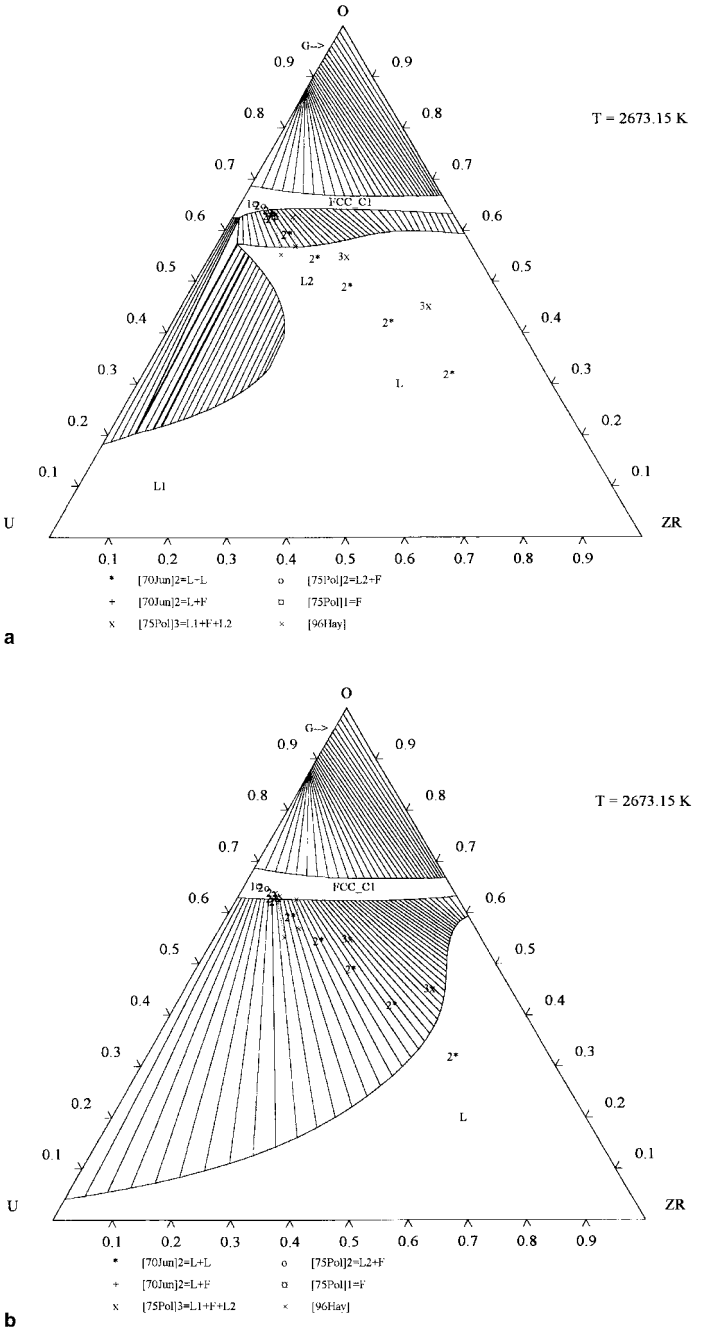

Fig. 24. (a) Calculated (parameters a) and experimental O–U–Zr phase diagram at 2673 K. (b) Calculated (parameters b) and experimental O–U–Zr phase diagram at 2673 K.

whole temperature and composition range by an appropriate calculation code. The most characteristical sections have been calculated by using the calculation code GEMINI2 (Gibbs Energy MINImizer) [98] and compared to the available experimental information by using the two sets of parameters. An important vertical section $UO_{1.7}$–$ZrO_{0.54}$ (Fig. 11(a) and (b)) was calculated: the composition $UO_{1.7}$ has been selected to represent a mean value of UO_{2-x} for the interpretation of the Hayward and George experiments at high temperatures [96]. A more accurate work would require one to let vary the composition of UO_{2-x} versus temperature,

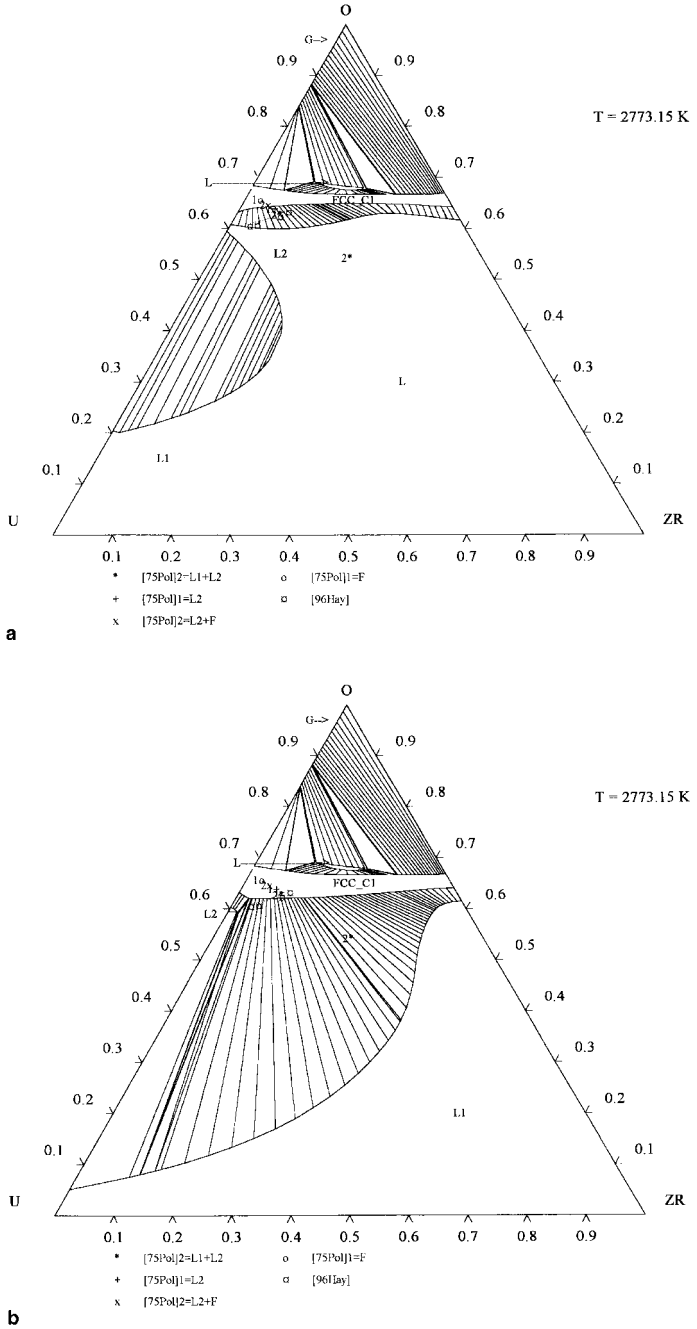

Fig. 25. (a) Calculated (parameters a) and experimental O–U–Zr phase diagram at 2773 K. (b) Calculated (parameters b) and experimental O–U–Zr phase diagram at 2773 K.

but the plot of a vertical section UO_{2-x}-α(Zr–O) with x as variable is not of current use. Sixteen isothermal sections in the temperature range 1073–2973 K (Figs. 12–27) are also presented.

The liquidus of the vertical section $UO_{1.7}$–$ZrO_{0.54}$ of Fig. 11(a) is in very good agreement with the experimental results of Hayward and George [95,96] (2373–2873 K) and Skokan [90] (2073–2373 K). Moreover, this section explains the temperature difference observed for the triphasic equilibrium L + fcc_C1 + hcp_A3, given as 2113 K by Politis [85] and 2173 K by Skokan [90]. In fact, in a ternary system, a triphasic region is not

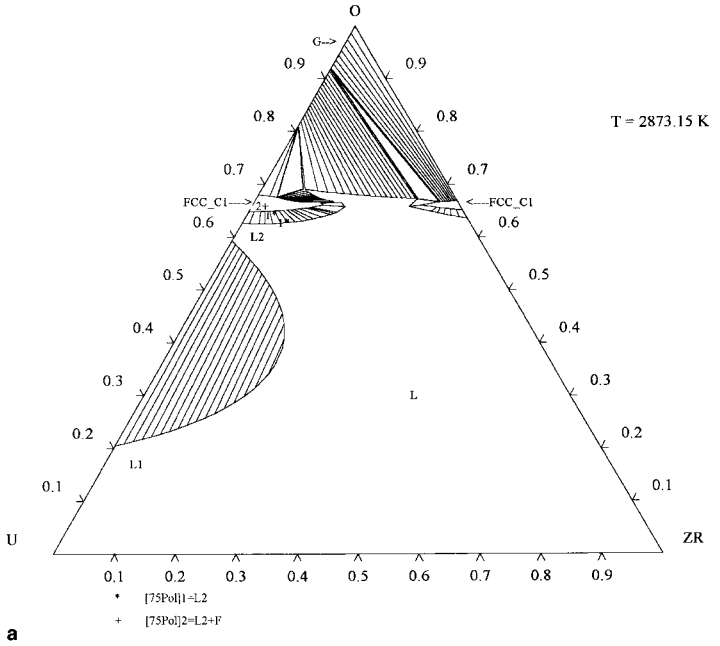

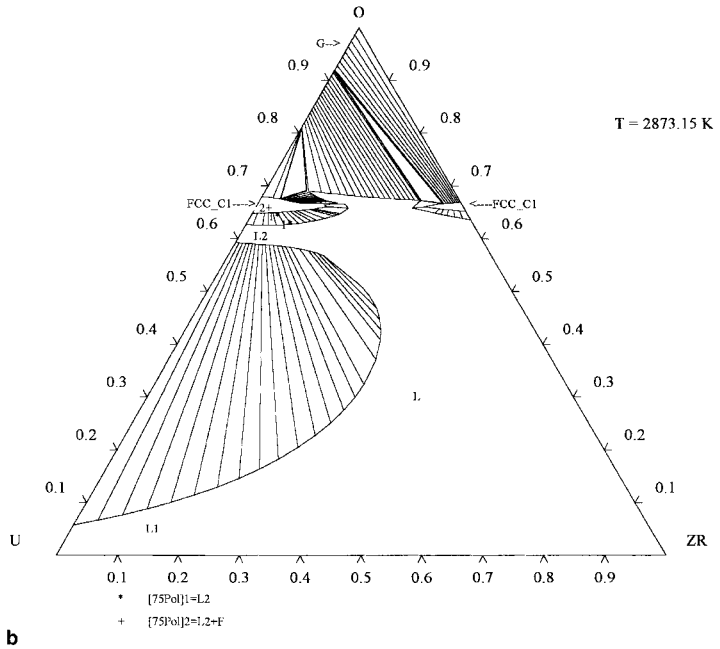

Fig. 26. (a) Calculated (parameters a) and experimental O–U–Zr phase diagram at 2873 K. (b) Calculated (parameters b) and experimental O–U–Zr phase diagram at 2873 K.

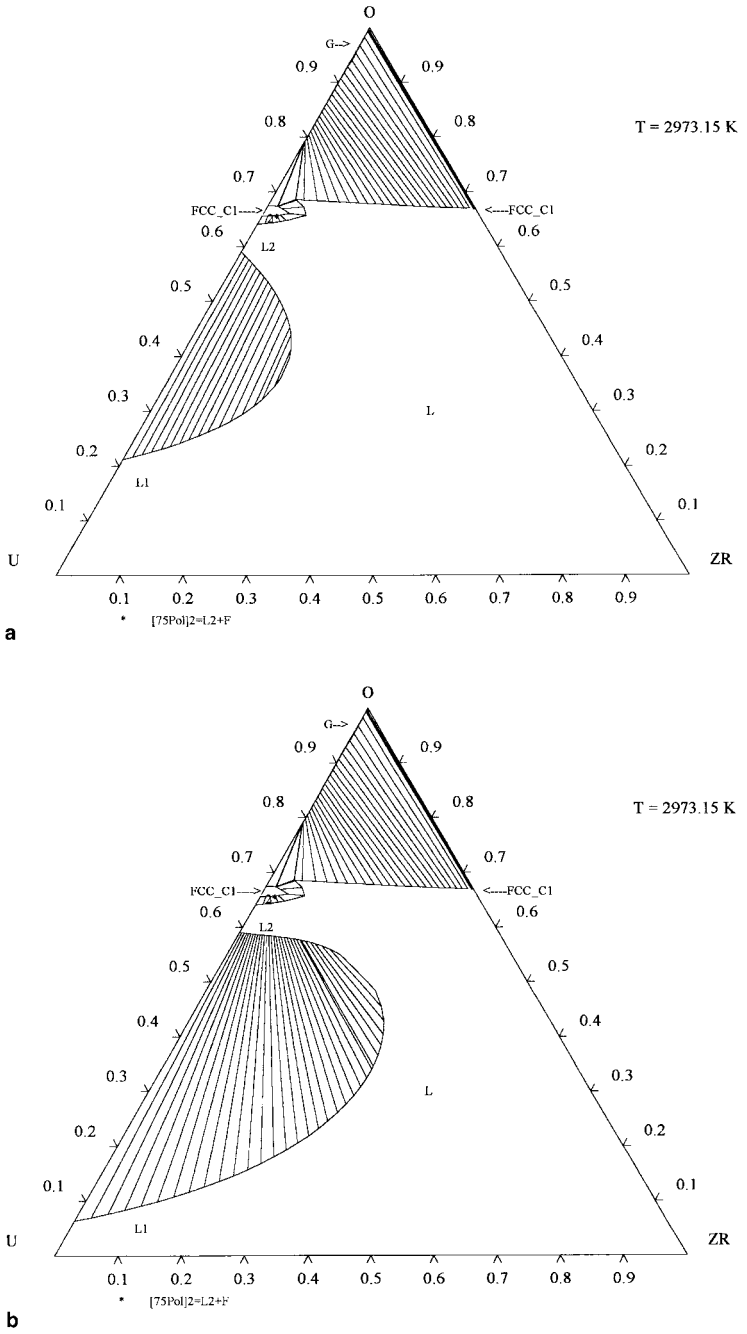

Fig. 27. (a) Calculated (parameters a) and experimental O–U–Zr phase diagram at 2973 K. (b) Calculated (parameters b) and experimental O–U–Zr phase diagram at 2973 K.

represented by a simple line as in a binary system, but by a surface limited by other one or two-phase regions. Thus, the transition temperature L + fcc_C1/L + fcc_C1 + hcp_A3 decreases when UO_2 increases, which is in agreement with both experimenters. This section do not show any miscibility gap in the liquid phase. In opposite, the pseudo-binary phase diagram $UO_{1.7}$–$ZrO_{0.54}$ presented in Fig. 11(b) shows a miscibility gap in agreement with the diagram of Politis [85]. However, the calculated monotectic temperature is higher than the one proposed by Politis [85]. It can be the result of an excessive stabilization of the fcc_C1 solid

solution with respect to the liquid phase, due to an important deviation from the ideal stoichiometry for oxygen. Further work on the modelling of the ternary fcc_C1 phase will be undertaken only when other more important discrepancies in the liquid will have been resolved.

The comparison between the calculated and experimental information is the same in the temperature range 1073–1773 K for the two set of parameters (a) and (b). The agreement between the calculated topology and the experimental two- and three-phase regions is satisfactory at $T = 1273$ K [85,87,91,93] and 1373 K (Saller et al. [84]). The existence of a wide two-phase regions in the UO_{2-x} region seems improbable due to the extent of the non-stoichiometry of the fcc_C1 phase. The exact position of the bcc_A2 composition in the triphasic domain should be accurately determined and not simply extrapolated. The calculated one has a higher zirconium content than the extrapolated one by experimenters, but is rapidly lowered at lowest temperatures (1073 K, 873 K). The uranium content in the hcp_A3 (α-ZrO) solid solution should be also determined more accurately. The topology of the calculated sections agrees with the one of Yamanaka et al. [92] at $T = 1673$ K, Politis [85] and Hofman and Politis [87] at 1773 K, although the experimental phase boundaries are still unaccurate.

The topology of the calculated isothermal sections is identical in the temperature range 1873–2373 K for the two set of parameters (a) and (b). For the case (a), the calculated solubility of oxygen in uranium–zirconium rich alloys is in good agreement with those of Hofman and Politis [87] at 2273 K and Skokan [90] in the temperature range 2073–2373 K, but higher than the one determined by Maurisi et al. [97] and Politis [85]. The agreement is inversed for the case (b).

The topology differs from 2473 K to very high temperatures. For the case (a), a liquid miscibility gap appears at 2473 K and is present up to 3000 K, but never reaches the UO_2–Zr line. The monophasic liquid domain is very important. The agreement is very satisfactory with the most recent values determined by Hayward and George [96] in the temperature range 2373 K–2773 K, and very poor with the pseudo-binary section of Politis [85]. For the case (b), the agreement is satisfactory with the pseudo-binary section of Politis [85] in the temperature range 2373–2673 K, but completely destroyed with the results of Hayward and George [96]. The liquid miscibility gap appears only at 2735 K, which is the O–U monotectic temperature, and extends towards higher zirconium contents when temperature increases, beyond the UO_2–Zr line. At very high temperature (>2773 K), the monotectic temperature raises with zirconium content, and the diphasic liquid + (U, Zr)UO_{2-x} domain is much larger. The main disagreement in the second case is the monotectic temperature on the pseudo-binary section, which is located between 2773 and 2873 K, and thus higher than the one determined by Politis [85], around 2673 K. However, we can underline that, as for the triphasic equilibrium L↔hcp_A3 + fcc_C1, the triphasic equilibrium L↔L + fcc_C1 is not obligatorily represented by a line in the vertical section UO_2–α(ZrO), and may have a non-negligible temperature range.

Thus, before doing complementary work on the ternary interaction parameters, which could perhaps simulate a different curve for the solubility of oxygen in U–Zr alloys (equilibrium L/L + (U, Zr)UO_{2-x}), it is necessary to understand the apparent discrepancies between the different experimental results in the intermediate temperature range 2373–2673 K. The extent of the ternary liquid miscibility gap at higher temperature (>2700 K) is tightly linked to the phase diagram at lower temperature on a thermodynamic point of view.

Moreover, possible disagreements may come from the modelling of the fcc_C1 ternary phase. The limits of this phase with respect to oxygen have to be analyzed in the ternary system, because the thermodynamic stability of this phase can modify the phase boundaries. Around 2773 K, the Gibbs energies of all phases in equilibrium are on a very similar level, and thus, a little variation of anyone may have a great influence on the phase diagram.

Important efforts remain to be made on the real interpretation of the experiments in term of equilibrium phase diagram: first, do other components (W, ...) play a disturbing effect? secondly, is the real thermodynamic equilibrium reached or at least approached with no further significant modification? third, do not the post-observation of quenched samples introduce a system effect, associated to a complex solidification process and a strong thermal gradient?

The aim of this work is to extend the discussion between all experimenters or modellers involved in this field. It will allow to assess the available experimental information and to obtain a set of self-consistent thermodynamic parameters for the O–U–Zr ternary system, which is a 'key-system' for nuclear safety.

This theoretical work associated to new experimental work in progress in the framework of the CIT (Corium Interaction and Thermochemistry) European project will then allow to evaluate the final ternary interaction parameters allowing to calculate the real equilibrium phase diagram.

5. Conclusion

We present in this work a complete thermodynamic modelling of the O–U–Zr system made from the critical evaluation of all the limiting binary and pseudo-binary sub-systems, and of the ternary experimental information. The non-stoichiometry of the oxide solid solution (U, Zr)$O_{2\pm x}$ is taken into account. The Gibbs energy

Appendix A. Gibbs energy parameters of condensed pure elements ('Lattice-stabilities') and stoichiometric substances in the ternary O–U–Zr system

$$G(\mathrm{Sub}) - G(\mathrm{Ref}) = a_k + b_k T + c_k T\,\mathrm{Log}(T) + d_k T^2 + e_k T^3 + f_k T^{-1} + i_k T^7 + j_k T^{-9} \quad \text{for } T_k < T < T_{k+1}.$$

	Ref	T_k	a_k i_k	b_k j_k	c_k	d_k	e_k	f_k
Element								
O (L)	O_2 (G)	298.15	−2648.9	+31.44				
O (fcc_C1)	O_2 (G)	298.15	+50 000					
U (ort_A20)	SER	298.15	−8407.734	+130.95515	−26.9182	$+1.25156 \times 10^{-3}$	-4.42605×10^{-6}	+38 568
		955	−22 521.8	+292.121093	−48.66			
U (tet)	SER	298.15	−5156.136	+106.976316	−22.841	-1.084475×10^{-2}	$+2.7889 \times 10^{-8}$	+81 944
		941.5	−14 327.309	+244.16802	−42.9278			
U (bcc_A2)	SER	298.15	−752.767	+131.5381	−27.5152	-8.35595×10^{-3}	$+9.67907 \times 10^{-7}$	+204 611
		1049	−4698.365	+202.685635	−38.2836			
U (L)	SER	298.15	+3947.766	+120.631251	−26.9182	$+1.25156 \times 10^{-3}$	-4.42605×10^{-6}	+38 568
		955	−1016 663.3	+281.797193	−48.66			
U (fcc_C1)	U (ort_A20)	298.15	+50 000					
U (hcp_A3)	U (ort_A20)	298.15	+5000					
Zr (fcc_C1)	Zr (hcp_A3)	298.15	+50 000					
Zr (ort_A20)	Zr (hcp_A3)	298.15	+31 591.91					
Zr (tet)	Zr (hcp_A3)	298.15	+29 999.34					
Zr (bcc_A2)	SER	298.15	−525.5386908 $-7.6142894 \times 10^{-11}$	+124.9457	−25.607406	-3.40084×10^{-4}	$-9.7289735 \times 10^{-9}$	+25 233
		2128	−30 705.95469	+264.2841628 $+1.276057535 \times 10^{+32}$	−42.144			
Zr (hcp_A3)	SER	298.15	−7827.594691	+125.64905	−24.1618	-4.37791×10^{-3}		+34 971
		2128	−26 085.92071	+262.7241828 $-1.34289552 \times 10^{+31}$	−42.144			
Zr (L)	SER	298.15	+10 320.09531 $+1.6275 \times 10^{-22}$	+116.568238	−24.1618	-4.37791×10^{-3}		+34 971
		2128	−8281.259691	+253.812609	−42.144			

Appendix A (Continued)

	Ref	T_k	a_k i_k	b_k j_k	c_k	d_k	e_k	f_k
Substance								
U_3Zr_7 (S)	U (ort_A20) Zr (hcp_A3)	298.15	−13 333.3	+13.9324				
UO_2 (fcc_C1)	SER	298.15	−1112 055.29	+433.85191	−74.6514	-6.10305×10^{-3}	$+1.7213 \times 10^{-7}$	$+6.4901 \times 10^{+5}$
		1500	−1707 426.87	+4369.945	−604.679	+0.205276	-1.583148×10^{-5}	$+1.265805 \times 1-0^{+8}$
		2670	−1303 255.56	+1218.637	−167.038			
UO_2 (L)	SER	298.15	−1018 368.29	+403.26101	−74.6514	-6.10305×10^{-3}	$+1.7213 \times 10^{-7}$	$+6.4901 \times 10^{+5}$
		1500	−1613 739.87	+4339.541	−604.679	+0.205276	-1.583148×10^{-5}	$+1.265805 \times 1-0^{+8}$
		2598	−1115 877.41	+868.30348	−130.959			
UO_2 (tet)	UO_2 (fcc_C1)	298.15	+5000					
UO_2 (mon)	UO_2 (fcc_C1)	298.15	+131 625.07					
UO_2 (hcp_A3)	UO_2 (fcc_C1)	298.15	+120 000*					
UO_3 (S)	SER	298.15	−1272 189.68	+507.83504	−88.701	-7.2448×10^{-2}		$+5.04515 \times 10-^{+5}$
UO_3 (bcc_A2)	UO_3 (S)	298.15	+1000 000*					
U_3O_8 (S)	SER	298.15	−3674 536.03	+1620.26249	−279.267	-1.374×10^{-2}		$+2.1558 \times 10^{+6}$
U_4O_9 (S)	SER	298.15	−4627 561.25	+1840.33759	−319.163	-2.48455×10^{-2}		$+1.9801 \times 10^{+6}$
ZrO_2 (fcc_C1)	SER	298.15	−1113 681	+491.486437	−80			
ZrO_2 (mon)	SER	298.15	−1126 367.62	+426.0761	−69.6218	-3.7656×10^{-3}		$+7.0291 \times 10^{+5}$
ZrO_2 (hcp_A3)	ZrO_2 (mon)	298.15	+140 000*					
ZrO_2 (tet)	SER	298.15	−1121 646.51	+479.515703	−78.1			
ZrO_2 (L)	SER	298.15	−1031 671.62	+391.93310	−69.6218	-3.7656×10^{-3}		$+7.0291 \times 10^{+5}$
		1478	−1035 025.34	+450.83609	−78.1			
		2208	−1083 380.54	+641.362639	−100			
ZrO_3 (bcc_A2)	O_2 (G) Zr(hcp_A3)	298.15	−978 407.60*	+332.0716*	−18.267556*	$+1.160192 \times 10^{-3}$*	$+6.4 \times 10^{-8}$*	$+7.825 \times 10^{+5}$*

Appendix B. Gibbs energy parameters of condensed solutions in the ternary O–U–Zr system

$$L_{j,k:l} = \Sigma_v L^{(v)}_{j,k:l}(y_j - y_k)^v \qquad L^{(v)}_{j,k:l} = a^{(v)}_{j,k:l} + b^{(v)}_{j,k:l}T.$$

Phase	Formula	Excess interaction parameters		
		Name	(a)	(b)
Liquid	$[O_1, O_2U_1, O_2Zr_1, U_1, Zr_1]\ \langle L\rangle$	$L^0[O_1, O_2U_1]\langle L\rangle$	−128 172.29	
		$L^1[O_1, O_2U_1]\langle L\rangle$	−95443.89	
		$L^0[O_1, O_2Zr_1]\langle L\rangle$	0	
		$L^0[O_1, U_1]\langle L\rangle$	0	
		$L^0[O_1, Zr_1]\langle L\rangle$	0	
		$L^0[O_2U_1, U_1]\langle L\rangle$	+32 057.50	+43 830.81
		$L^1[O_2U_1, U_1]\langle L\rangle$	−39 679.44	−58 301.77
		$L^2[O_2U_1, U_1]\langle L\rangle$	−54 694.14	−30 394.73
		$L^0[O_2U_1, O_2Zr_1]\langle L\rangle$	−2479.09	
		$L^0[O_2U_1, Zr_1]\langle L\rangle$	0*	+70 000*
		$L^0[O_2Zr_1, Zr_1]\langle L\rangle$	−14 537.78	
		$L^1[O_2Zr_1, Zr_1]\langle L\rangle$	−25 619.98	
		$L^2[O_2Zr_1, Zr_1]\langle L\rangle$	−39 753.77	
		$L^0[U_1, O_2Zr_1]\langle L\rangle$	+50 000*	
		$L^0[U_1, Zr_1]\langle L\rangle$	+16 181.73	
		$L^1[U_1, Zr_1]\langle L\rangle$	+51.48	
		$L^2[U_1, Zr_1]\langle L\rangle$	+4064.16	
fcc_C1	$[O_1, Va]_2[U_1, Zr_1, Va]_1\ \langle fcc\_C1\rangle$	$L^0[O_1, Va]_2\ [U_1]_1\langle fcc\_C1\rangle$	+88 353.17 − 32.37686T	+63 331.87 − 20.43520T
		$L^1[O_1, Va]_2\ [U_1]_1\langle fcc\_C1\rangle$	+42858.36	+43 425.53
		$L^0[O_1, Va]_2\ [Zr_1]_1\langle fcc\_C1\rangle$	+6926.92	
		$L^1[O_1, Va]_2\ [Zr_1]_1\langle fcc\_C1\rangle$	−10 696.34	
		$L^0[O_1, Va]_2\ [Va_1]_1\langle fcc\_C1\rangle$	0	
		$L^0[O_1]_2\ [U_1, Zr_1]_1\langle fcc\_C1\rangle$	+35 978.53 − 5.3254T	
		$L^0[O_1]_2\ [U_1, Va]_1\langle fcc\_C1\rangle$	+184 216.70 + 135.95271T	
		$L^1[O_1]_2\ [U_1, Va]_1\langle fcc\_C1\rangle$	−1422 742.46	
		$L^2[O_1]_2\ [U_1, Va]_1\langle fcc\_C1\rangle$	+782 551.16	
		$L^0[O_1]_2\ [Zr_1, Va]_1\langle fcc\_C1\rangle$	0	
		$L^0[Va_1]_2\ [U_1, Zr_1]_1\langle fcc\_C1\rangle$	+35 978.53 − 5.3254T*	
		$L^0[Va_1]_2\ [U_1, Va]_1\langle fcc\_C1\rangle$	0	
		$L^0[Va_1]_2\ [Zr_1, Va]_1\langle fcc\_C1\rangle$	0	
Tetragonal	$[O]_2[U_1, Zr_1]_1\ \langle tet\rangle$	$L^0[O_1]_2[U_1, Zr_1]_1\langle tet\rangle$	+22 980.94	
		$L^1[O_1]_2[U_1, Zr_1]_1\langle tet\rangle$	−11 040.70	
Monoclinic	$[O]_2[U_1, Zr_1]_1\ \langle mon\rangle$	$L^0[O_1]_2[U_1, Zr_1]_1\ \langle mon\rangle$	0	
hcp_A3	$[O_1, Va]_2[U_1, Zr_1]_1\ \langle hcp\_A3\rangle$	$L^0[O_1, Va]_2\ [U_1]_1\ \langle hcp\_A3\rangle$	0*	
		$L^0[O_1, Va]_2\ [Zr_1]_1\ \langle hcp\_A3\rangle$	−185 881.63 + 15.38370*T	
		$L^1[O_1, Va]_2\ [Zr_1]_1\ \langle hcp\_A3\rangle$	−8945.82	
		$L^2[O_1, Va]_2\ [Zr_1]_1\ \langle hcp\_A3\rangle$	+45 913.67	
		$L^0[O_1]_2\ [U_1, Zr_1]_1\ \langle hcp\_A3\rangle$	−6623.53*	
		$L^0[Va_1]_2\ [U_1, Zr_1]_1\ \langle hcp\_A3\rangle$	−6623.53	
bcc_A2	$[O_1, Va]_3[U_1, Zr_1]_1\ \langle bcc\_A2\rangle$	$L^0[O_1, Va]_3\ [U_1]_1\ \langle bcc\_A2\rangle$	0*	
		$L^0[O_1, Va]_3\ [Zr_1]_1\ \langle bcc\_A2\rangle$	−617 159.34 + 96.93941*T	
		$L^0[O_1]_3\ [U_1, Zr_1]_1\ \langle bcc\_A2\rangle$	0*	

Appendix B (Continued)

Phase	Formula	Excess interaction parameters		
		Name	(a)	(b)
		$L^0[Va_1]_3\ [U_1, Zr_1]_1\ \langle bcc\_A2\rangle$	+16 610.14	
		$L^1[Va_1]_3\ [U_1, Zr_1]_1\ \langle bcc\_A2\rangle$	+3670.28	
		$L^2[Va_1]_3\ [U_1, Zr_1]_1\ \langle bcc\_A2\rangle$	+1820.25	
		$L^3[Va_1]_3\ [U_1, Zr_1]_1\ \langle bcc\_A2\rangle$	−1503.13	
		$L^4[Va_1]_3\ [U_1, Zr_1]_1\ \langle bcc\_A2\rangle$	+3461.55	
Tet	$[U_1, Zr_1]_1\ \langle tet\rangle$	$L^0[U_1, Zr_1]_1\ \langle tet\rangle$	0	
Ort_A20	$[U_1, Zr_1]_1\ \langle ort\_A20\rangle$	$L^0[U_1, Zr_1]_1\ \langle ort\_A20\rangle$	0	

Note: case (a) – high solubility of oxygen in liquid uranium (O–U); ideal interaction O_2U_1–Zr_1 (O–U–Zr); case (b) – low solubility of oxygen in liquid uranium (O–U); positive interaction O_2U_1–Zr_1 (O–U–Zr).

parameters (unary, binary and ternary) of all condensed phases are evaluated from an optimization procedure and constitute a part of the TDBCR [1]. Consequently, the provisional equilibrium phase diagram of the ternary O–U–Zr system can be calculated in the whole temperature and composition range. Characteristic vertical and isothermal sections have been calculated by using the GEMINI2 code [98] and compared to the available experimental information.

Due to the apparent controversy in the experimental information, especially concerning the solubility of oxygen in uranium–zirconium liquid alloys and the extent of the liquid miscibility gap, the equilibrium phase diagram was calculated by using two different sets of interaction parameters. The two versions allow to reproduce separately the two incompatible families of experimental points, but differ on only O–U and O–U–Zr interaction parameters.

Future efforts will be made on the interpretation of the existing or newly available experiments in terms of thermodynamic equilibrium in order to validate an improved version of the true equilibrium phase diagram, and also to bring explanations to the apparent experimental inconsistencies.

Acknowledgements

This work was executed under the multi-partner research contract 'CIT Project / FI4S-CT96-0032' co-financed by the European Commission under the Euratom specific Nuclear Fission Safety programme 1994-1998. The authors wish to thank the partners of this contract, IPSN, EC-JRC, ENEA, FZK, THERMODATA, SIEMENS, CEA, EDF, FRAMATOME, for valuable technical discussions.

References

[1] P.Y. Chevalier, E. Fischer, B. Cheynet, A. Rivet, G. Cenerino, Proc. Int. Conf. on Thermodynamics of Alloys, Marseille, France, 2–5 September 1996; J. Chim. Phys. 94 (1997) 849.
[2] B. Cheynet, Proc. Int. Conf. on Computerized Metallurgical Databases, Cincinnati, Ohio, USA, 10–16 October 1987 (Met. Soc. Inc., USA, 1988, pp. 28–40).
[3] H.L. Lukas, E.Th. Henig, B. Zimmermann, CALPHAD 1 (3) (1977) 225.
[4] B. Sundman, J. Agren, J. Phys. Chem. Solids 42 (1981) 297.
[5] O. Redlich, A.T. Kister, Ind. Eng. Chem. 40 (1948) 345.
[6] The SGTE Casebook, in: K. Hack (Ed.), Thermodynamics at Work, Materials Modelling Series, The Institute of Materials, 1996.
[7] A.T. Dinsdale, CALPHAD 15 (4) (1991) 317.
[8] E.M. Levin, C.R. Robbins, H.F. McMurdie, Phase Diagrams for Ceramists, Am. Ceram. Soc., 1964.
[9] E.M. Levin, C.R. Robbins, H.F. McMurdie, Phase Diagrams for Ceramists 1969 Supplement (Figures 2067–4149), Am. Ceram. Soc., 1969.
[10] E.M. Levin, H.F. McMurdie, Phase Diagrams for Ceramists 1975 Supplement (Figures 4150–4999), Am. Ceram. Soc., 1975.
[11] R.S. Roth, T. Negas, L.P. Cook, Phase Diagrams for Ceramists, vol. IV (Figures 5000–5590), Am. Ceram. Soc., 1981.
[12] P.L. Blum, P. Guinet, H. Vaugoyeau, C.R. Acad. Sci. 257 (22) (1963) 3401.
[13] F.A. Shunk, Constitution of Binary Alloys, second supplement, McGraw-Hill, New York, 1969.
[14] J.L. Bates, US At. Energy Comm., HW-81603, 1964, pp. 2.15–2.23.
[15] R.P. Elliott, Constitution of Binary Alloys, first supplement, McGraw-Hill, New York, 1965.
[16] A.E. Martin, R.K. Edwards, J. Phys. Chem. 69 (5) (1965) 1788; R.K. Edwards, A.E. Martin, Thermodynamics of Nuclear Materials, vol. II, IAEA, Vienna, 1966, p. 423.
[17] J.L. Bates, J. Am. Ceram. Soc. 49 (7) (1966) 395.

[18] P. Guinet, H. Vaugoyeau, P.L. Blum, C.R. Acad. Sci., Ser. C 263 (1966) 17; rapport CEA-R3060, CENG, Section de Métallurgie, Novembre 1966.
[19] M.J. Bannister, J. Nucl. Mater. 24 (1967) 340.
[20] R.J. Ackermann, E.G. Rauh, M.S. Chandrasekharaiah, J. Phys. Chem. 73 (4) (1969) 762.
[21] R.E. Latta, R.E. Fryxell, J. Nucl. Mater. 35 (1970) 195.
[22] S.P. Garg, R.J. Ackermann, J. Nucl. Mater. 88 (1980) 309.
[23] R.J. Ackermann, E.G. Rauh, High Temp. Sci. 4 (1972) 496.
[24] S.P. Garg, R.J. Ackermann, Metall. Trans. A 8 (1977) 239.
[25] W.E. Wang, D.R. Olander, J. Am. Ceram. Soc. 76 (5) (1993) 1242.
[26] A. Kotlar, P. Gerdanian, M. Dodé, J. Chem. Phys. 65 (1968) 687.
[27] T. Matsui, K. Naito, J. Nucl. Mater. 56 (1975) 327.
[28] A. Caneiro, J.P. Abriata, J. Nucl. Mater. 126 (1984) 255.
[29] Y. Saito, J. Nucl. Mater. 51 (1974) 112.
[30] D.I. Marchidan, S. Matei Tanasescu, Rev. Roum. Chim. 17 (9) (1972) 1487.
[31] D.I. Marchidan, S. Matei Tanasescu, Rev. Roum. Chim. 18 (10) (1973) 1681.
[32] D.I. Marchidan, S. Matei Tanasescu, Rev. Roum. Chim. 19 (9) (1974) 1435.
[33] D.I. Marchidan, S. Matei Tanasescu, Rev. Roum. Chim. 20 (11/12) (1975) 1365.
[34] N.A. Javed, J. Nucl. Mater. 43 (1972) 219.
[35] V.J. Wheeler, J. Nucl. Mater. 39 (1971) 315.
[36] C. Picard, P. Gerdanian, J. Nucl. Mater. 99 (1981) 184.
[37] S. Aronson, J. Belle, J. Chem. Phys. 29 (1) (1958) 151.
[38] M. Tetenbaum, P.D. Hunt, J. Nucl. Mater. 34 (1970) 86.
[39] T. Lindemer, T.M. Bessman, J. Nucl. Mater. 130 (1985) 473.
[40] E.H.P. Cordfunke, R.J.M. Konings, G. Prins, P.E. Potter, M.H. Rand, Thermochemical data for reactor materials and fission products, Eur. Contract ETSN-0005-NL (February 1988).
[41] A. Pattoret, PhD thesis, Université Libre de Bruxelles (1969).
[42] M. Hansen, K. Anderko, Constitution of Binary Alloys, second edition, McGraw-Hill, New York, 1958.
[43] R.F. Domagala, D.J. McPherson, J. Metals, Trans. AIME, February (1954) 238.
[44] R.J. Ackermann, S.P. Garg, E.G. Rauh, J. Am. Ceram. Soc. 60 (7/8) (1977) 341.
[45] J.P. Abriata, J. Garcès, R. Versaci, Bulletin of Alloy Phase Diagrams 7 (1986) 2.
[46] B. Holmberg, A. Magneli, Acta Chem. Scand. 12 (6) (1958) 1341.
[47] B. Holmberg, T. Dagerhamn, Acta Chem. Scand. 15 (4) (1961) 919.
[48] E. Gebhardt, H.D. Seghezzi, W. Dürrschnabel, J. Nucl. Mater. 4 (3) (1961) 255.
[49] R. Ruh, H.J. Garrett, J. Am. Ceram. Soc. 50 (5) (1957) 257.
[50] R.J. Ackermann, S.P. Garg, E.G. Rauh, J. Am. Ceram. Soc. 61 (5/6) (1978) 275.
[51] T. Tanabe, M. Tanaka, S. Imoto, Surf. Sci. 187 (1987) 499.
[52] A.N. Kornilov, I.M. Ushakova, S.M. Skuratov, G.P. Shveikin, Dok. Akad. Nauk SSSR 186 (4) (1969) 831.
[53] G. Boureau, P. Gerdanian, High Temp.–High Press. 2 (1970) 681.
[54] G. Boureau, P. Gerdanian, J. Phys. Chem. Solids 45 (2) (1984) 141.
[55] R.J. Ackermann, S.P. Garg, E.G. Rauh, High Temp. Sci. 11 (1979) 199.
[56] E.G. Rauh, S.P. Garg, High Temp. Sci. 14 (1981) 121.
[57] O. Relave, P.Y. Chevalier, B. Cheynet, G. Cenerino, in: F.H. Hayes (Ed.), Proc. Int. Conf. on User Aspects of Phase Diagrams, Joint Research Centre, Petten, The Netherlands, 25–27 June 1990, The Institute of Metals, 1991, p. 55.
[58] M. Yashima, T. Koura, Y. Du, M. Yoshimura, J. Am. Ceram. Soc. 79 (2) (1996) 521.
[59] W.A. Lambertson, M.H. Mueller, J. Am. Ceram. Soc. 36 (11) (1953) 367.
[60] N.M. Voronov, E.A. Voitekhova, A.S. Danilin, Proc. Second Genova Conf. 6 (1958) 221.
[61] G.M. Wolten, J. Am. Chem. Soc. 80 (1958) 4772.
[62] P.E. Evans, J. Am. Ceram. Soc. 43 (9) (1960) 443.
[63] I. Cohen, B.E. Schaner, J. Nucl. Mater. 9 (1) (1963) 18.
[64] L.G. Wisnyi, S.W. Pijanowski, Knolls Atomic Power Laboratory (USA) Report, KAPL-1702 (1957).
[65] K.A. Romberger, C.F. Baes, H.H. Stone, J. Inorg. Nucl. Chem. 29 (1967) 1619.
[66] J.O.A. Pashoal, H. Kleykamp, F. Thümmler, J. Nucl. Mater. 151 (1987) 10.
[67] C.A. Alexander, J.S. Ogden, R.Y. Lee, High Temp. Mater. Sci. 33 (1995) 3.
[68] V. Stolyarova, A. Shilov, M. Shultz, J. Nucl. Mater. 247 (1997) 41.
[69] R.I. Sheldon, D.E. Peterson, Bull. Alloy Phase Diagrams 10 (2) (1989) 165.
[70] H. Okamoto, J. Phase Equil. 14 (2) (1993) 267.
[71] D. Summers-Smith, J. Inst. Met. 83 (1954–1955) 277.
[72] J. Philibert, Y. Adda, C.R. Acad. Sci., 23rd December (1957) 2507.
[73] J.F. Duffey, C.A. Bruch, Trans. Met. Soc. AIME, February (1958) 17.
[74] S.T. Zegler, USAEC Rep.ANL-6055 (1962).
[75] L. Leibowitz, E. Veleckis, R.A. Blomquist, A.D. Pelton, J. Nucl. Mater. 154 (1988) 145.
[76] T. Ohmichi, private communication.
[77] T. Ogawa, T. Iwai, J. Less-Common Meter. 170 (1991) 101.
[78] A. Maeda, Y. Suzuki, T. Ohmichi, J. Alloys Compounds 179 (1992) L25.
[79] M. Akabori, A. Itoh, T. Ogawa, F. Kobayashi, Y. Suzuki, J. Nucl. Mater. 188 (1992) 249.
[80] B.W. Howlett, A.G. Knapton, Second UN Int. Conf. on Peaceful Use of Atomic Energy, Geneva, 6, 1958, p. 104.
[81] M. Kanno, M. Yamawaki, T. Koyama, N. Morioka, J. Nucl. Mater. 154 (1988) 154.
[82] L. Leibowitz, R.A. Blomquist, A.D. Pelton, J. Nucl. Mater. 167 (1989) 76.
[83] K. Nagarajan, R. Babu, C.K. Mathews, J. Nucl. Mater. 203 (1993) 221.
[84] H.A. Saller, F.A. Rough, J.M. Fackelmann, A.A. Bauer, J.R. Doig, BMI-1023 (1955).
[85] C. Politis, Gesellschaft für Kernforschung M.B.H., Karlsruhe, KFK 2167 (Oct. 1975) 1–53.
[86] P. Hofman, H. Holleck, C. Politis, A. Skokan, Gesellschaft für Kernforschung M.B.H., Karlsruhe, KFK 2242 (Feb. 1976) 1–3.

[87] P. Hofman, C. Politis, J. Nucl. Mater. 87 (1979) 375.
[88] D.L. Hagrman, G.A. Reymann, R.E. Mason, NUREG/CR-0479, TREE-1280, Rev. 2, R3 and R4, Inc., Idaho Falls, Idaho 83415 (August 1981).
[89] E.F. Junke, J.F. White, GEMP-731 (1970).
[90] A. Skokan, Proc. Fifth Int. Meeting on Thermonuclear Reactor Safety, Karlsruhe, 9–13 September 1984.
[91] S. Yamanaka, M. Katsura, M. Miyake, S. Imoto, S. Kawasaki, J. Nucl. Mater. 130 (1985) 524.
[92] S. Yamanaka, M. Katsura, S. Imoto, M. Miyake, Inorg. Chim. Acta 140 (1987) 127.
[93] M. Miyake, M. Katsura, S. Yamanaka, J. Nucl. Mater. 154 (1988) 123.
[94] P. Hofman, S.J.L. Hagen, G. Schanz, A. Skokan, Kernforschungszentrum Karlsruhe, KFK 4485 (Jan. 1989).
[95] P. Hayward, I.M. George, J. Nucl. Mater. 208 (1994) 35.
[96] P. Hayward, I.M. George, J. Nucl. Mater. 232 (1996) 1.
[97] A. Maurisi, C. Gueneau, P. Perodeaud, B. Schneider, O. Dugne, F. Valin, G. Bordier, Proc. Int. Conf. EUROMAT, October 1996.
[98] B. Cheynet, J.N. Barbier, P.Y. Chevalier, A. Rivet, E. Fischer, in: V. Farber (Ed.), Proc. Int. Conf. CALPHAD XXI, Jerusalem, Israel, 14–19 June 1992; CALPHAD 16 (4) (1992) 339.